

Helical trilayer graphene: a moiré platform for strongly-interacting topological bands

Li-Qiao Xia,^{1,*} Sergio C. de la Barrera,^{1,2,*} Aviram Uri,^{1,*} Aaron Sharpe,³

Yves H. Kwan,⁴ Ziyan Zhu,⁵ Kenji Watanabe,⁶ Takashi Taniguchi,⁷ David Goldhaber-Gordon,^{8,5} Liang Fu,¹ Trithep Devakul,^{8,1} and Pablo Jarillo-Herrero¹

¹*Department of Physics, Massachusetts Institute of Technology, Cambridge, MA, USA*

²*Department of Physics, University of Toronto, Toronto, Ontario, Canada*

³*Materials Physics Department, Sandia National Laboratories, Livermore, CA, USA*

⁴*Princeton Center for Theoretical Science, Princeton University, Princeton NJ 08544, USA*

⁵*Stanford Institute for Materials and Energy Sciences, SLAC National Accelerator Laboratory, Menlo Park, CA 94025*

⁶*Research Center for Electronic and Optical Materials, National Institute for Materials Science, 1-1 Namiki, Tsukuba 305-0044, Japan*

⁷*Research Center for Materials Nanoarchitectonics, National Institute for Materials Science, 1-1 Namiki, Tsukuba 305-0044, Japan*

⁸*Department of Physics, Stanford University, Stanford, CA 94305, USA*

(Dated: October 20, 2023)

Quantum geometry of electronic wavefunctions results in fascinating topological phenomena. A prominent example is the intrinsic anomalous Hall effect (AHE) in which a Hall voltage arises in the absence of an applied magnetic field. The AHE requires a coexistence of Berry curvature and spontaneous time-reversal symmetry breaking [1]. These conditions can be realized in two-dimensional moiré systems with broken xy -inversion symmetry (C_{2z}) that host flat electronic bands [2–25]. Here, we explore helical trilayer graphene (HTG) [26–33], three graphene layers twisted sequentially by the same angle forming two misoriented moiré patterns. Although HTG is globally C_{2z} -symmetric, surprisingly we observe clear signatures of topological bands. At a magic angle $\theta_m \approx 1.8^\circ$, we uncover a robust phase diagram of correlated and magnetic states using magnetotransport measurements. Lattice relaxation leads to large periodic domains in which C_{2z} is broken on the moiré scale. Each domain harbors flat topological bands with valley-contrasting Chern numbers $\pm(1, -2)$ [29–31, 33]. We find correlated states at integer electron fillings per moiré unit cell $\nu = 1, 2, 3$ and fractional fillings $2/3, 7/2$ with the AHE arising at $\nu = 1, 3$ and $2/3, 7/2$. At $\nu = 1$, a time-reversal symmetric phase appears beyond a critical electric displacement field, indicating a topological phase transition. Finally, hysteresis upon sweeping ν points to first-order phase transitions across a spatial mosaic of Chern domains [34] separated by a network of topological gapless edge states. We establish HTG as an important platform that realizes ideal conditions for exploring strongly interacting topological phases and, due to its emergent moiré-scale symmetries, demonstrates a novel way to engineer topology.

INTRODUCTION

The combination of strong electronic correlations and non-trivial band topology is fertile ground for exotic electronic phenomena. Driven by Berry curvature and orbital magnetization, the spontaneous emergence of the AHE in non-magnetic materials is a notable example. It requires a periodic system with broken PT and time-reversal (T) symmetries [35] (here, P is the inversion symmetry). Two-dimensional moiré materials are ideal for realizing these conditions since constituent layers with specific symmetries can be combined in a controlled way to engineer both the electronic band structure and its topology. Indeed, the AHE was realized in different C_{2z} -broken moiré platforms, including graphene-based systems [2–8, 10–15, 17–19] and transition-metal dichalcogenides [16, 20–24], where at least one of the van der Waals layers intrinsically breaks C_{2z} . These systems rely on a single moiré to generate flat bands and strong

correlations, while layers with broken C_{2z} give rise to Berry curvature.

Three layers of graphene, however, twisted with two independent angles, θ_{12} and θ_{23} , between the top two layers (1 and 2) and bottom two layers (2 and 3), respectively, unlock a new engineering degree of freedom by combining more than one moiré lattice. While much of the two-angle space (θ_{12}, θ_{23}) is filled with mutually incommensurate moiré lattices forming moiré quasicrystals [36], some angle combinations will give rise to periodic domains on the moiré scale. Some commensurate combinations of twist angles, $p\theta_{12} = q\theta_{23}$ (p, q integers) [26, 37, 38], may locally escape quasiperiodicity, particularly once lattice relaxation is taken into account. Here, we demonstrate moiré engineering of local periodicity with $(p, q) = (1, 1)$ equi-angle HTG, which we refer to as HTG throughout. In HTG, large moiré-periodic domains are formed by lattice relaxation, supporting electronic Bloch bands, emergent broken symmetries, and Chern numbers defined within each domain. Although HTG is made purely of C_{2z} -symmetric components and is globally C_{2z} -symmetric, within the periodic domains the system breaks C_{2z} on the moiré scale, generating

* These authors contributed equally.

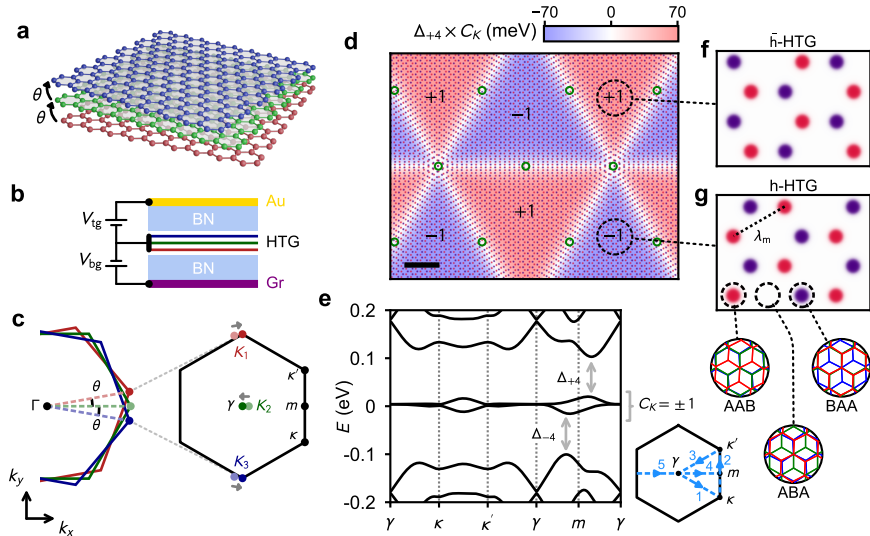


Fig. 1. Helical trilayer graphene. **a**, Schematic of the magic-angle HTG structure comprising three layers of graphene rotated in the same direction by the same twist angle, $\theta \approx 1.8^\circ$. **b**, Circuit diagram of HTG surrounded by two hBN dielectric layers and top and bottom gate electrodes (Au and graphite, Gr) kept at electric potentials V_{tg} , V_{bg} relative to HTG. **c**, The rotated Brillouin zones of the three monolayers (left). Without lattice relaxation, the three Dirac points (light-colored dots) lie on an arc. Including lattice relaxation (grey arrows), in the h-HTG and \bar{h} -HTG domains they lie on a straight line, forming a periodic moiré Brillouin zone. **d**, Moiré structure of HTG including lattice relaxation. Crimson and purple dots represent AA stacking of the top and bottom pairs of proximate layers, respectively. The small atomic lattice relaxation is enough to form moiré-periodic domains (h-HTG and \bar{h} -HTG) hosting topological flat bands with large gaps, $\Delta_{\pm 4}$, to remote bands. Scale bar is 50 nm. Background color represents $\Delta_{\pm 4} \times C_K$ calculated for the local shift δ between the two moiré lattices, where C_K is the total Chern number per spin of the pair of flat bands in valley K . Green circles indicate centers of approximate C_{2z} rotation symmetry. **e**, Local non-interacting band structure in the h-HTG domain for valley K . **f-g**, Moiré arrangement in the \bar{h} -HTG (**f**) and h-HTG (**g**) periodic domains, where C_{2z} is broken on the moiré scale. Circular callouts show the local atomic stacking of the three graphene layers in different regions.

Berry curvature and non-trivial topology. Furthermore, the moiré bands can be sufficiently flat to spontaneously break time-reversal symmetry (TRS), leading to our observation of the AHE at certain fillings. Our observation of the AHE in HTG brings to light the importance of local symmetries on length scales comparable to the interparticle distance, $n^{-1/2}$.

HELICAL TRILAYER GRAPHENE

The three graphene layers in HTG, rotated sequentially by the same angle θ (Fig. 1a), form two moiré patterns between adjacent layer pairs. The two moiré lattices share the same lattice constant, $\lambda_m \approx a/\theta \approx 7.8$ nm for $\theta = 1.8^\circ$, and are misoriented by θ (here, $a = 0.246$ nm is the atomic lattice constant of graphene). The misorientation between the two moiré patterns produces a position-dependent relative shift between them that is approximately periodic. This supermoiré (or moiré of moiré) pattern has a lattice constant $\lambda_{sm} \approx \lambda_m/\theta \approx 250$ nm. In the absence of lattice relaxation, the two moiré patterns are mutually incommensurate and the effective structure for low-energy electrons is a moiré quasicrystal [36]. Lattice relaxation on the moiré scale is most prominent at small angles, $\theta \lesssim 1^\circ$, and is typically less important for larger angles [39]. However, even at

angles as large as $\theta = 1.8^\circ$, relaxation can have a profound effect on the supermoiré scale, favoring certain relative shifts between the two moiré patterns. The relaxed structure of HTG forms large moiré-periodic domains, termed h-HTG and \bar{h} -HTG, that are related by a C_{2z} transformation [29, 31]. Figures 1d,f,g show the calculated relaxed moiré structure (Methods L). Importantly, within each periodic domain, C_{2z} symmetry is spontaneously broken, allowing for Berry curvature and non-trivial topology.

The local non-interacting band structure within a domain is described by a pair of narrow-bandwidth topological bands (per spin and valley), touching at three Dirac points (κ , κ' , and γ) and separated by large gaps of order 70 meV from the remote bands (Figs. 1c,e). Each pair of flat bands carries a total valley-contrasting Chern number $C_{K,K'} = \pm 1$ (Fig. 1e) [29, 31]. Electronic interactions are predicted to give rise to correlated insulators at integer fillings, in the form of spontaneous flavor ferromagnetism in spin (\uparrow, \downarrow), valley (K, K'), and Chern-sublattice (A, B) space with Chern numbers $C = \pm(1, -2)$ [33]. We will refer to the Chern-sublattice basis as sublattice for short hereinafter. In states where h-HTG and \bar{h} -HTG bands have different Chern numbers per spin or valley the network of domain walls between them hosts gapless edge modes [29, 31]. Relaxation into periodic moiré domains comes at a cost of increased

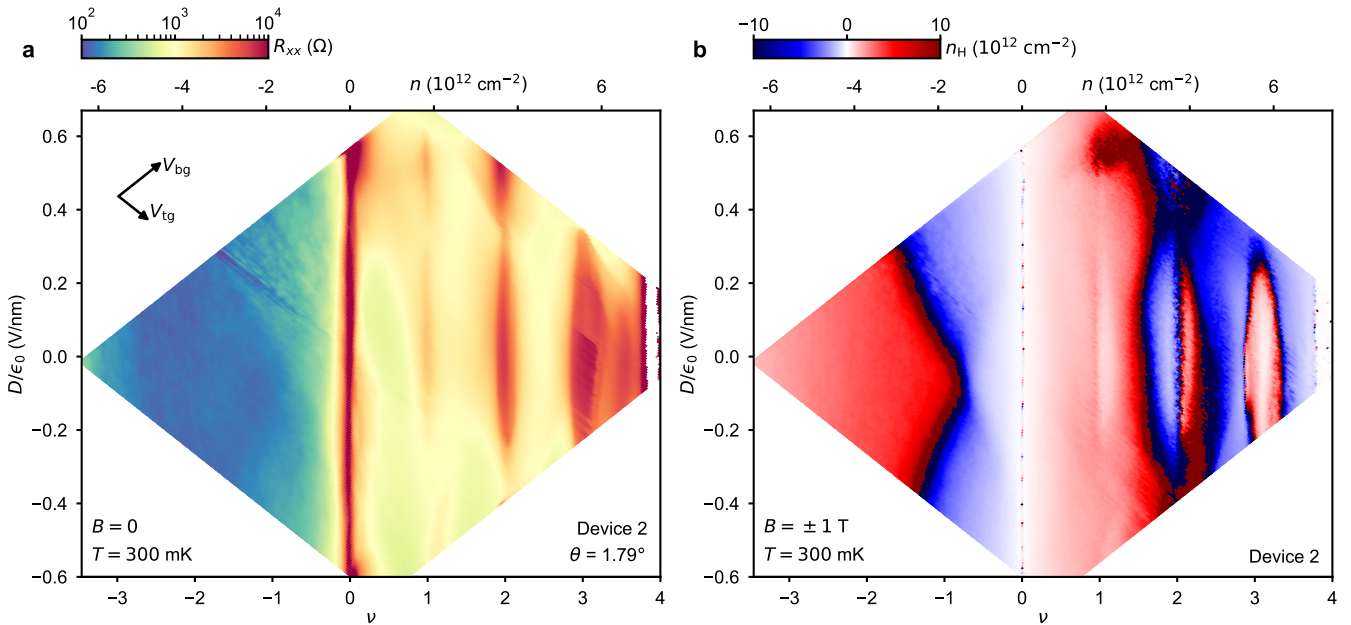


Fig. 2. Strong electronic interactions. **a**, R_{xx} versus ν and D measured at $B = 0$ and $T = 300 \text{ mK}$, showing resistance peaks at charge neutrality ($\nu = 0$), at the moiré band gap ($\nu = 4$), and at the correlated states ($\nu = 1, 2, 3$ and $7/2$). **b**, Hall density n_H versus ν and D , acquired from antisymmetrizing R_{yx} at $B = \pm 1 \text{ T}$ and $T = 300 \text{ mK}$.

moiré aperiodicity within the domain walls [29]. The overall structure of HTG is therefore a triangular tiling of moiré-periodic domains (on the scale of a few hundred nanometers) that are separated by gapless moiré-aperiodic domain walls (Fig. 1d). The global structure has approximate C_{2z} -symmetry, as h-HTG and \bar{h} -HTG are C_{2z} counterparts (see Figs. 1f,g).

In the absence of TRS breaking, both valleys are equally occupied and the total Chern number is zero. Electron-electron interactions facilitated by the quenched kinetic energy of the flat bands can lift the flavor degeneracy, similar to magic-angle graphene [40–42], spontaneously breaking TRS and yielding a net Chern number within each periodic domain [2, 3].

CORRELATED STATES

To probe the transport properties of HTG, we constructed dual-gated devices encapsulated by hexagonal boron nitride (hBN) (Methods A, Extended Data Fig. 1). By applying voltages to the top and bottom gates (V_{tg} and V_{bg} , respectively, see Fig. 1b), we controlled the electron density, n , and the perpendicular electric displacement field, D , independently, while performing four-terminal magneto-transport measurements (Methods B). The data shown throughout were measured using Device 2 unless stated otherwise.

Figure 2a shows the longitudinal resistance R_{xx} versus n and D measured at $B = 0$ and $T = 300 \text{ mK}$, where B is the applied out-of-plane magnetic field. The large

resistance peak at $n = 7.45 \times 10^{12} \text{ cm}^{-2}$ indicates the gap between the flat and remote moiré bands at a filling of four electrons per moiré unit cell, $\nu = nA_{uc} = 4$, where A_{uc} is the area of the moiré unit cell. This reflects a twist angle of $\theta = 1.79^\circ$ (Methods C). Additional resistance peaks appear at integer fillings $\nu = 1, 2$, and 3, indicative of flavor-symmetry-broken correlated electronic states. We observed similar behavior in two more devices – see Extended Data Figs. 3a and 4a (for the appearance of correlated states in HTG devices with twist angles away from the magic angle see Methods D and Table 2). Fig. 2b shows the Hall density, n_H (Methods F), measured versus n and D . For electron-doping, $n > 0$, and small D , n_H shows “resetting” behavior around $\nu = 1$ and 2, where n_H drops towards zero [41, 42]. Additionally, we find Van Hove singularities (VHSs) near $\nu = 1.5$ and 2.2 [43]. The rightmost oval-shaped discontinuity in n_H near $\nu = 3$ does not reflect VHSs. Rather, they are the result of the strong AHE in this region (see details below) that we do not account for in our extraction of n_H .

Both the R_{xx} and n_H maps reveal pronounced electron-hole asymmetry. Correlated states only appear on the electron side, an observation we find consistently in all of our HTG devices (see Extended Data Figs. 3, 4, 8, and Extended Data Table 2). Our current microscopic theory does not account for this strong asymmetry. We can, however, use the shape of the valence band VHS in the measured Hall density map to infer effective microscopic parameters for our model. Compared to the electron side, the hole side is better described (phenomenologically) by a larger ratio of renormalized

Fermi velocity to interlayer hopping strength (see Methods I), resulting in a larger bandwidth and diminished correlation effects at $\theta \approx 1.8^\circ$.

ANOMALOUS HALL EFFECT

Figures 3a-f show the measured field-symmetrized R_{xx} and field-antisymmetrized R_{yx} as we sweep B up and down at different temperatures (see Methods E for a description of the symmetrization and antisymmetrization procedure). We observe nonzero Hall resistance at $B = 0$ accompanied by pronounced magnetic hysteresis consistent with ferromagnetism in the vicinity of both $\nu = 1$ and 3. Considering the small intrinsic spin-orbit coupling in graphene, the ferromagnetism in our system is almost certainly of orbital origin rather than spin alone [44, 45], as was shown [7, 34] in other graphene-based moiré systems in which AHE was previously reported. Combined with the topological flat bands (Fig. 1e) [29–31], this points to orbital ferromagnetism driven by Berry curvature in valley-polarized states [33]. While R_{yx} is not quantized in our measurements, we would only expect to observe quantization from a single Chern domain. The magnitude of $|R_{yx}| \gtrsim 1.5 \text{ k}\Omega$ at $B = 0$ in our experiment reflects the net effect of multiple domains and the network of gapless domain walls between the R_{yx} contacts. We find multiple Barkhausen jumps and hysteresis in R_{yx} -versus- B loops that persists up to a temperature of $T_{\text{phys}} \approx 7.5 \text{ K}$. The R_{yx} discontinuity at $B = 0$ disappears at a Curie temperature of $T_C \approx 10.5 \text{ K}$ (see also Methods G and Extended Data Fig. 2), which is the highest reported among graphene-based moiré systems (see Extended Data Table 1).

Notably, we find the AHE at $\nu = 1, 3$ in two additional devices with similar twist angles (see Extended Data Fig. 3 and Extended Data Fig. 4), demonstrating the robustness of the AHE in HTG. Apart from non-trivial band topology, another key requirement for interaction-driven orbital magnetism is that the ground state favored by strong correlations spontaneously breaks TRS and has a net Chern number. In twisted monolayer-bilayer graphene (tMBG), previous studies suggested that a close competition exists between different many-body ground states, including a valley-polarized state that breaks TRS and an intervalley-coherent state that preserves it [5, 8]. This potentially makes the AHE in tMBG more sensitive to strain and twist angle disorder [11, 46]. In contrast, the robustness of the AHE in HTG suggests that valley-polarized states are strongly favored at odd fillings. This is in alignment with strong-coupling theory of HTG [33].

Figure 3g provides an overview of the AHE in our system by plotting the difference ΔR_{yx} between R_{yx} taken at $B = \pm 60 \text{ mT}$ after training at high fields, $\pm 1 \text{ T}$, respectively. In the ranges $0.9 \lesssim \nu \lesssim 1.1$ and $2.8 \lesssim \nu \lesssim 3.3$, we find nonzero ΔR_{yx} indicating AHE, corroborated by the B -sweep hysteresis loops. In contrast, the correlated state near $\nu = 2$ shows no AHE, indicating a state

that preserves TRS. At this filling fraction theory points to a quantum valley-Hall state within the periodic domains [33]. The approximate symmetry of the AHE about $D = 0$ indicates that it does not rely on aligning the graphene trilayer to a substrate (see also Extended Data Fig. 1d).

There is a weaker ΔR_{yx} hot spot near $\nu = 2/3$ and $D/\epsilon_0 = 0.3 \text{ V/nm}$ (Fig. 3g). Figure 3e shows R_{yx} versus B measured at $\nu = 0.62$, $D = 0.41 \text{ V/nm}$ showing AHE. We note that at the same D -field there is no AHE at $\nu = 1$ (Fig. 3f), hence the AHE at fractional filling is a distinct state. This observation may indicate the presence of a topological charge density wave or fractional Chern insulator (see Methods J). The latter was predicted in HTG at $D=0$ [29]; However, it is unclear whether the HTG bands favor fractional Chern insulators at large D fields. Thus, further investigation is required to identify the ground state. The appearance of the $\nu = 2/3$ feature only at $D > 0$ may be due to a slight difference in the effective screening from the top and bottom gates.

Lastly, there is an isolated resistive state centered on $\nu = 7/2$ and $D = 0$ (see Fig. 2a), that emerges as a distinct feature at low temperatures (Extended Data Fig. 6), indicating a symmetry-broken phase. Furthermore, we find AHE that extends from $\nu = 3$ to beyond $\nu = 7/2$ (Extended Data Fig. 7b) indicating the nontrivial topology of this state. At this filling, our Hartree-Fock calculations find closely competing topological states that include charge density waves [47] and a tetrahedral antiferromagnet (Methods J).

INDICATIONS OF TOPOLOGICAL PHASE TRANSITIONS

In Fig. 2a the resistive peak at $\nu = 1$ centered at $D = 0$ disappears at $|D/\epsilon_0| \approx 0.35 \text{ V/nm}$ and reappears at higher $|D|$, suggestive of a phase transition involving a gap closure and re-opening. We do not find evidence for AHE at $|D/\epsilon_0| > 0.35 \text{ V/nm}$, hence the high- $|D|$ phases preserve TRS. A leading theoretical possibility suggested by recent Hartree-Fock calculations of HTG [33] is that at a critical displacement field D_c band inversion leads to a topological phase transition, with trivial bands emerging at $|D| > D_c$. While a gapped intervalley-coherent state is also expected to show similar transport signatures, this possibility is unlikely [29, 33]. We observe similar behavior of R_{xx} near $\nu = 2$, although at this filling both the high- and low- $|D|$ phases preserve TRS, also consistent with theory [33].

ELECTRICAL SWITCHING OF CHERN DOMAINS

By sweeping density in a fixed small magnetic field, $B \lesssim 0.2 \text{ T}$, we find that the sign of the AHE for a given ν depends on the sweep direction (Figs. 4a,b). This type of switching was suggested to be a result of a compe-

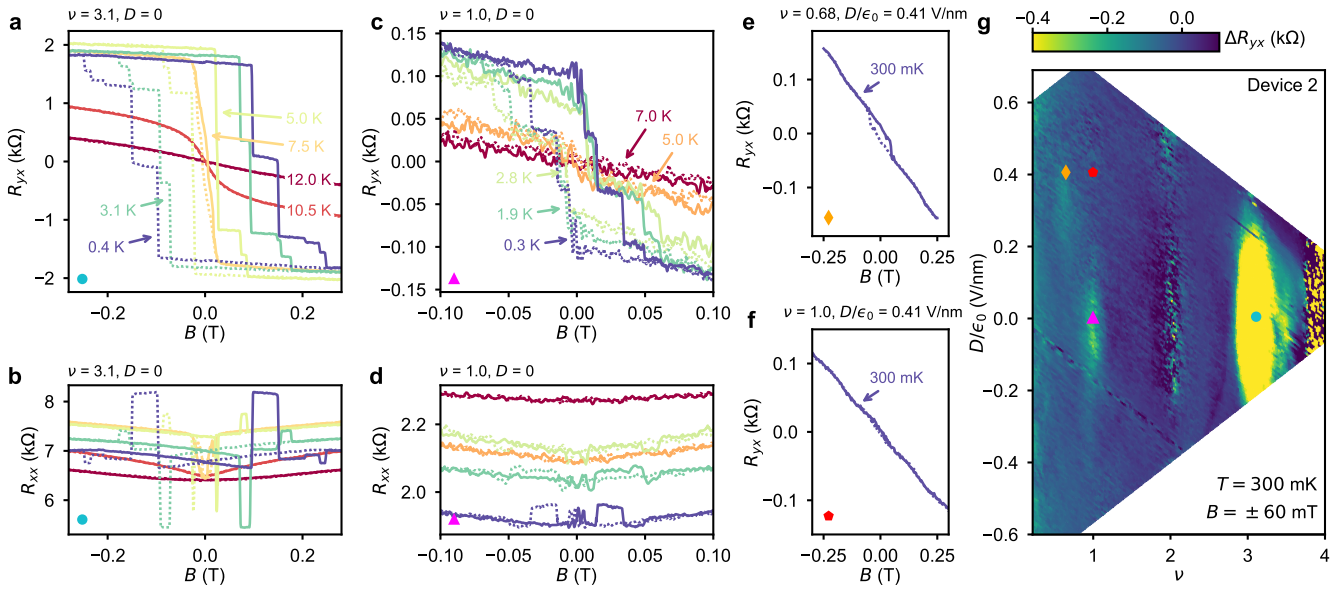


Fig. 3. Anomalous Hall effect. **a,b**, Field-antisymmetrized R_{yx} and field-symmetrized R_{xx} taken at $\nu = 3.1$ and $D = 0$ (cyan circle in **g**) while sweeping B up (solid) and down (dashed) at different temperatures as indicated. Temperature color code in **b** is identical to **a**. **c,d**, Same as **a,b**, taken at $\nu = 1$ (pink triangle in **g**). **e**, Same as **a**, taken at $\nu = 0.68$, $D/\epsilon_0 = 0.41$ V/nm (orange diamond in **g**), and $T = 300$ mK showing AHE near $\nu = 2/3$. **f**, Same as **e**, taken at the same D and T but at $\nu = 1$ (red pentagon in **g**) showing no AHE. **g**, Field-trained ΔR_{yx} measured at $T = 300$ mK and $B = \pm 60$ mT after training at $B = \pm 1$ T versus ν and D . Hot spots near $\nu = 1, 3$ and $\nu \approx 2/3$ indicate AHE.

tition between the different contributions to the orbital Zeeman energy, $-\mathbf{M} \cdot \mathbf{B}$ [48], where \mathbf{M} is the total orbital magnetization, directed out of the plane. M has two contributions [35]: the self-rotation magnetization, M_{SR} , due to the self-rotation of the electronic wavepacket, and the Chern magnetization, M_C , due to the center-of-mass motion of the wavepacket. The two can have opposite signs and they depend strongly on the chemical potential, allowing the total magnetization per valley to change sign as the density is swept. A calculation of the orbital magnetization $M(\nu)$ for the h-HTG domain, based on Hartree-Fock bands calculated at $\nu = 3$, is presented in Methods K, demonstrating the sign change required for the above switching mechanism.

The hysteresis in $R_{yx}(\nu)$ shown in Figs. 4a,b exists over a large density range. Notably, it is present only at low magnetic fields and disappears abruptly as $|B|$ is increased above a critical value $B_c \sim 0.2$ T. Moreover, when sweeping ν up (Fig. 4a), R_{yx} in the high positive field regime ($B > B_c$) is almost identical to R_{yx} in low negative field ($0 < B < B_c$). This phenomenology is strikingly similar to what was previously observed [34] in near-commensurate hBN-aligned magic-angle TBG and is distinct from the phenomenology observed in other orbital Chern insulators [5, 6, 12]. In the former, local magnetic imaging revealed a spatial pattern of domains with different Chern numbers in the low-field regime [34]. Our observation of a similar phenomenology in $R_{yx}(\nu, B)$ is not surprising, given the coexistence of h-HTG and \bar{h} -HTG domains that may have different Chern numbers at integer filling factors [33]. Below, we give a possible explanation for the observed unique hysteresis pattern.

We note, however, that the multiple domains, gapless domain walls, and the large number of degrees of freedom may give rise to complex magnetotransport behavior. Hence, the picture described below may be incomplete.

At $\nu = 3$, as a result of interaction-induced flavor polarization, seven of the eight flavors are filled, and one is empty. Figure 4c illustrates such a scenario. Because both A/B sublattices and h-HTG/ \bar{h} -HTG domains are related by C_{2z} , we expect that if the unfilled band in h-HTG is, say B -sublattice polarized, then in \bar{h} -HTG it would be A -sublattice polarized. Therefore, the sublattice polarization of the empty flavor is domain contrasting (Figs. 4c,d). We are now left with the assignment of valley and spin to the empty flavor in each domain. Because of the vanishingly small spin-orbit coupling in graphene we ignore the spin in the following discussion. At a nonzero magnetic field, one naively expects the system to minimize orbital-Zeeman energy by aligning the orbital magnetization of all the domains with the applied field. This can be achieved by polarizing h-HTG and \bar{h} -HTG domains to opposite valleys. However, due to the high valley-domain-wall energy cost [33], this arrangement is disfavored. Instead, all the domains polarize collectively to the same valley, breaking TRS, and forming an inter-domain antiferromagnetic (AFM) order (Figs. 4d,e) – a mosaic of Chern domains [34]. We denote the two possible AFM configurations as α and α' , corresponding to K and K' valley polarizations, respectively (Figs. 4c,d). The inevitable imbalance between h-HTG and \bar{h} -HTG domains in a real sample results in a small net orbital magnetization M_{net} that couples

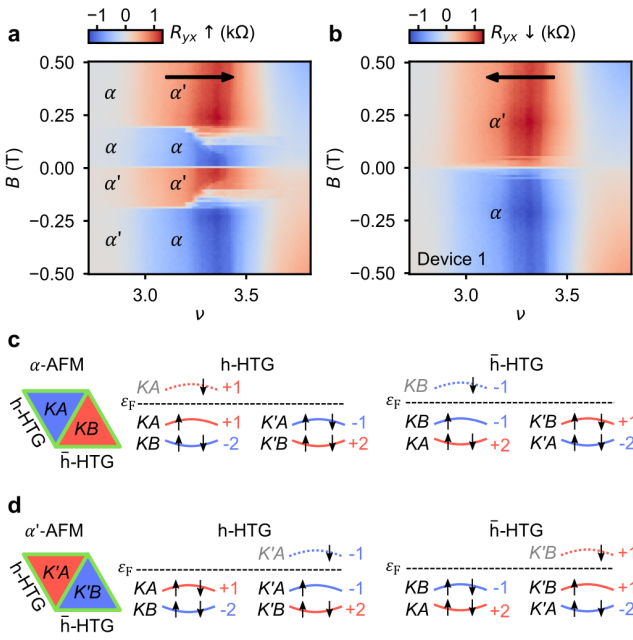


Fig. 4. Density-induced switching and Chern mosaic at $\nu = 3$. **a**, Field-antisymmetrized R_{yx} versus ν and B while sweeping ν up as fast axis, measured on Device 1 at $D/\epsilon_F = -0.15$ V/nm. The theoretical α and α' AFM configurations are indicated. **b**, Same as **a** only sweeping ν down. **c,d**, Schematic of the flavor-energetics in h-HTG and \bar{h} -HTG domains in the interacting picture for $\nu = 3$, describing the two AFM orders, α (**c**) and α' (**d**). At integer ν , interactions gap the Dirac points, forming eight bands with spin, valley, and sublattice flavors. The Chern numbers per band are indicated. At $\nu = 3$ seven flavors are filled, and one is empty (dashed). The two triangles represent the h-HTG and \bar{h} -HTG domains (empty flavor is indicated). Red (blue) indicates total Chern number 1 (-1) while green indicates gapless regions at $\nu = 3$.

to the applied magnetic field via orbital-Zeeman energy, $\delta\epsilon = -\mathbf{M}_{\text{net}} \cdot \mathbf{B}$. The uncompensated AFM can therefore be switched between α and α' if B is applied anti-parallel to M_{net} and the Zeeman energy exceeds some coercive energy threshold, $|\delta\epsilon| > \Delta_c$.

We now describe Fig. 4a. At $\nu < 3$ and $B > 0$, M_{net} is aligned with B and system is in the α configuration. As the density is swept up through the $\nu = 3$ correlated gap, the total magnetization per domain switches sign abruptly (see Methods K) and so does M_{net} . At a high magnetic field, $B > B_c$, $|\delta\epsilon|$ exceeds the coercive energy Δ_c , and the system collectively switches to the α' configuration. In contrast, at low fields, $0 \leq B < B_c$, as ν is swept through the gap, $|\delta\epsilon| < \Delta_c$ and the AFM order cannot be flipped although M_{net} is anti-parallel to the field. This explains the opposite R_{yx} at high and low fields in Fig. 4a. Using the same argument, we can also understand why the small negative field regime, $-B_c < B < 0$, shows R_{yx} similar to the positive high field regime, $B > B_c$. At small negative field, the system is in the α' configuration to align M_{net} with the field. The system remains in the α' configuration also for $\nu > 3$

because $|\delta\epsilon| < \Delta_c$.

We now describe Fig. 4b showing R_{yx} while sweeping ν down. Above some critical filling fraction, ν_c , the intradomain ferromagnetic order melts. Sweeping down from $\nu > \nu_c$ is akin to field-cooling a ferromagnet; As the system crosses ν_c and becomes ferromagnetic it chooses the energetically favorable AFM order which is α (α') for $B > 0$ ($B < 0$), see Fig. 4b.

Although the phenomenology we observe in Figs. 4a,b is similar to near-commensurate hBN-aligned magic-angle TBG [34], important differences exist between the two systems. Further work is therefore required to determine the precise dynamics underlying the observed transport behavior in Figs. 4a,b.

SCALE-DEPENDENT SYMMETRIES

It is instructive to consider the symmetries of a locally-periodic system at the length scale of the inter-particle distance, $n^{-1/2}$. For example, TBG is C_{2z} -symmetric at densities of order one electron per moiré unit cell, as embodied in the continuum approximation [49]. This accounts for the scarcity of AHE observations in hBN-misaligned TBG. In contrast, in hBN-aligned TBG, C_{2z} is broken by the inequivalence between the alignment of boron and nitrogen atoms with the graphene moiré unit cell. Since there exists no center of C_{2z} rotation anywhere in the lattice, this symmetry is broken everywhere, promoting non-trivial topology in the moiré bands. A similar situation exists in tMBG and in twisted transition-metal dichalcogenides. HTG is qualitatively different. C_{2z} is broken on the moiré scale despite the global C_{2z} symmetry of HTG. The global symmetry is expressed by the existence of h-HTG and \bar{h} -HTG domains with C_{2z} -related Chern numbers.

OUTLOOK

Our results demonstrate that engineering a super-moiré system to break C_{2z} on the moiré scale can induce topological bands that favor TRS-broken ground states at odd fillings. The Chern domains and network of gapless edge modes, together with the high T_C and the high yield of samples exhibiting the AHE, establish HTG as an ideal platform for exploring orbital magnetism with Chern domain walls. Owing to its relatively homogeneous charge distribution, near-ideal quantum geometry [29], and small interaction-induced dispersion [33], HTG is a promising platform for realizing exotic electronic phases [29, 47]. Our observation of an AHE at fractional filling factors, combined with the favorable conditions for zero-field fractional Chern insulating states [29], motivates further experimental and theoretical investigations of magic-angle HTG.

METHODS

A. Device fabrication

The van der Waals heterostructures were assembled in two parts using the standard dry-transfer technique. First, a hBN flake and a few-layer graphene strip were picked up by a poly(bisphenol A carbonate) stamp. This bottom stack was released onto a 285 nm SiO₂/Si substrate, followed by 12-hour vacuum annealing at 350 °C to remove polymer residues. Then, tip cleaning was performed using the Contact Mode of a Bruker Icon XR atomic force microscope to further clean the surface. A monolayer graphene flake was cut into three pieces using a confocal laser-cut setup. A second poly(bisphenol A carbonate) stamp was used to pick a hBN flake and the three graphene pieces subsequently. Before picking up the second and third pieces of graphene, the stage was rotated by 1.8° in the same direction to realize a helical stacking order. The pickup of graphene was done at room temperature to avoid the relaxation of the twist angle. The top stack was released onto the bottom stack at 150 °C – 170 °C.

The Hall bar was defined in a bubble-free region, identified under an atomic force microscope. Patterns were defined using an Elionix ELS-HS50 electron-beam lithography system. A metallic top gate (25 nm - 65 nm Au with a 2 nm - 5 nm Cr or Ti adhesion layer) was deposited using a Sharon thermal evaporator. The device was connected using one-dimensional contacts (63 nm - 75 nm Au with a 2 nm - 5 nm Cr adhesion layer) [50]. Finally, the device was etched into a Hall bar geometry using reactive-ion etching.

B. Electrical transport measurements

Low-temperature electrical transport measurements were carried out in a helium-3 refrigerator with an 8 T perpendicular superconducting magnet and a base temperature of about 290 mK. A homemade twisted-pair copper tape filter with ~ 20 MHz cutoff frequency [51] was thermally anchored at base temperature to guarantee the electron temperature of the device is the same as the phonon temperature. DC voltages were applied to the top and bottom gates using Keithley 2400/2450 source-measure units. The AC excitation of 1 nA – 10 nA at 16 Hz – 24 Hz was applied using SR830 or SR860 lock-in amplifiers. The corresponding AC currents and voltages were measured using SR830 or SR860 lock-in amplifiers, preamplified using DL-1211 current preamplifiers, and DL-1201 voltage preamplifiers. The temperature was measured using a calibrated CX-1010-CU-HT-0.1L thermometer. $n = (\epsilon_{\text{BN}}\epsilon_0/e)(V_{\text{bg}}/d_{\text{bg}} + V_{\text{tg}}/d_{\text{tg}})$ and $D = (\epsilon_{\text{BN}}\epsilon_0/2)(V_{\text{bg}}/d_{\text{bg}} - V_{\text{tg}}/d_{\text{tg}})$ define n and D relations to V_{bg} and V_{tg} , where $\epsilon_{\text{BN}} = 3$ is the relative dielectric constant of hBN, ϵ_0 is the vacuum permittivity, e is the elementary charge, and d_{bg} (d_{tg}) is the thickness of the bottom (top) hBN.

Dilution refrigerator measurements were performed in a Leiden Cryogenics CF-900 using a custom probe. The measurement lines are equipped with electronic filtering at the mixing chamber stage to obtain a low electron temperature in the device and reduce high-frequency noise. There are two stages of filtering: the wires are first passed through a cured mixture of epoxy and bronze powder to filter GHz frequencies, then low-pass RC filters mounted on sapphire plates filter MHz frequencies. Samples were mounted using a Kyocera custom 32-contact ceramic leadless chip carrier (drawing PB-44567-Mod with no nickel sticking layer under gold, to reduce magnetic effects). Stanford Research Systems SR830 lock-in amplifiers with NF Corporation LI-75A voltage preamplifiers were used to perform four-terminal resistance measurements. A 1 GΩ bias resistor was used to apply an AC bias current of up to 5 nA RMS at a frequency of 6.451 Hz. Keithley 2400 source-measure units were used to apply voltages to the gates.

C. Twist angle determination

Band structure calculations for the h-HTG and \bar{h} -HTG domains show large moiré band gaps at $\nu = \pm 4$, while the domain walls remain gapless throughout the spectrum. At $\nu = \pm 4$, we expect the domain walls to form a metallic network shunting the gapped periodic domains and lowering the resistance at these fillings somewhat, compared with a homogeneous insulating system. Nevertheless, we can still clearly identify resistive peaks at $\nu = 4$ and Landau levels emerging from the band extrema. We therefore use the features at $\nu = \pm 4$ to extract a twist angle for each device, with $n_{\nu=\pm 4} = \pm 8 \sin^2 \theta / \sqrt{3}a^2 \approx \pm 8\theta^2 / \sqrt{3}a^2$, using $a = 0.246$ nm as the lattice constant for graphene.

We calibrate the twist angles for our HTG devices using the densities from which Landau levels emerge at integer fillings, particularly from $|\nu| = 4$ (Extended Data Fig. 5). We fit a series of integer slopes to the measured Landau level gaps (dips in R_{xx} emerging from $\nu = -4, 0, +4$) and resistive states at partial fillings (R_{xx} peaks at $\nu = 1, 2, 3$), using the density of $|\nu| = 4$, $n_{\nu=\pm 4}$, as a free parameter. The best fit across all fillings and sloped features yields for device 2 $n_{\nu=\pm 4} = 7.45 \pm 0.17 \times 10^{12} \text{ cm}^{-2}$, corresponding to $\theta = 1.79 \pm 0.02^\circ$. Errors are estimated by aligning the collection of R_{xx} features to the left and right edges of each feature (R_{xx} minima for Landau level gaps or peaks

of correlated states). See Table 2 for the twist angles and error estimates of the other devices (errors estimated from R_{xx} peaks at integer filling for cases without clear Landau levels), along with a summary of the filling fractions ν for which correlated R_{xx} features and the AHE in R_{yx} are observed. The preponderance of correlated features and observations of the AHE clearly increase as the twist angle approaches 1.79° , though the precise behavior for angles larger than $\sim 1.8^\circ$ remains to be explored in detail. This evolution of correlated features is especially evident in measurements of R_{xx} plotted versus ν for several devices in Extended Data Fig. 8.

We note that in the case of a slight mismatch between the two twist angles, $\theta_{12} \neq \theta_{23}$, the system relaxes to a structure similar to the equi-angle one, only with a smaller supermoiré unit cell (see Methods M). Transport measurements only allow us to extract the resulting local twist angle θ in the periodic domains, which is between θ_{12} and θ_{23} .

D. HTG at other twist angles

In addition to the three main devices reported here, we fabricated other equi-angle HTG devices at various twist angles ranging between 1.6° and 2.0° . Extended Data Fig. 8 shows selected $R_{xx}(\nu)$ traces at constant D -fields, as indicated. It reveals the range of twist angles that support correlated phases that appear as R_{xx} peaks near integer ν . The results are summarized in Table 2. We find correlated states in the range $1.7^\circ \lesssim \theta \lesssim 1.8^\circ$ with the $\nu = 2$ correlated phase surviving to the lowest twist angle.

E. Symmetrization and antisymmetrization

All the presented R_{xx} and R_{yx} data were symmetrized and antisymmetrized, respectively, with respect to the applied out-of-plane magnetic field B . Specifically, $R_{xx} = (R_{xx}^{\text{raw}}(B) + R_{xx}^{\text{raw}}(-B))/2$ and $R_{yx} = (R_{yx}^{\text{raw}}(B) - R_{yx}^{\text{raw}}(-B))/2$, where raw indicates raw data. This allows us to compensate for non-ideal Hall bar geometry and for anisotropies that we found to be significant and ubiquitous in HTG. In measurements where B is the fast sweep axis, such as in Figs. 3a-f, the symmetrization and antisymmetrization were performed between curves of opposite sweep direction, so that $R_{yx} = (R_{yx}^{\text{raw}\uparrow}(B) - R_{yx}^{\text{raw}\downarrow}(-B))/2$ and $R_{xx} = (R_{xx}^{\text{raw}\uparrow}(B) + R_{xx}^{\text{raw}\downarrow}(-B))/2$ (here, the arrows indicate the sweep direction of B). In measurements where B was the slow axis, such as Figs. 4a,b, the antisymmetrization was performed between curves with opposite constant B : $R_{yx} = (R_{yx}^{\text{raw}}(B) - R_{yx}^{\text{raw}}(-B))/2$ and similarly for R_{xx} .

F. Calculation of the Hall density

We extract the Hall density $n_H = -e^{-1}(dR_{yx}/dB)^{-1}$ from R_{yx} measurements taken at $\pm 1\text{ T}$ according to $n_H = -(B_+ - B_-)/e(R_{yx}(B_+) - R_{yx}(B_-))$, where $B_\pm = \pm 1\text{ T}$, e is the elementary charge, and $n_H > 0$ corresponds to electron doping. In a noninteracting system at low doping $n_H \approx n$, and is expected to diverge near a VHS. This is indeed the case for hole doping in our system. In contrast, on the electron doping, near $\nu = 1$ we find that n_H deviates below n , indicative of a flavor reset [41, 42], similar to magic-angle TBG (MATBG) and related moiré systems.

G. Extraction of Curie temperature

We extract T_C following Ref. [52] by plotting R_{yx}^2 versus $|B/R_{yx}|$ at different temperatures. Such a plot for Device 2 is shown in Extended Data Fig. 2, taken at $\nu = 2.9$ and $D = 0$. We take R_{yx} as a proxy for the magnetization M , reproducing an Arrott plot (M^2 versus M/H) [53]. The intercept of a linear extrapolation of the high-field regime determines the magnetic state. At temperatures $T < 10.5\text{ K}$ we find a positive intercept indicating a ferromagnetic phase. At $T = 10.5\text{ K}$ the intercept is approximately zero, and above this temperature, the intercept is negative indicating a transition to a paramagnetic phase, hence the Curie temperature is approximately 10.5 K .

H. Theoretical electronic band structure calculation

The theoretical single-particle band structure shown in Fig. 1e was calculated using the continuum model Hamiltonian [29]

$$H = \begin{pmatrix} v_0 \vec{\sigma}_\theta \cdot [\vec{k} - \vec{K}_1] + U & T(\vec{r} - \vec{d}_t) & 0 \\ T^\dagger(\vec{r} - \vec{d}_t) & v_0 \vec{\sigma} \cdot [\vec{k} - \vec{K}_2] & T(\vec{r} - \vec{d}_b) \\ 0 & T^\dagger(\vec{r} - \vec{d}_b) & v_0 \vec{\sigma}_{-\theta} \cdot [\vec{k} - \vec{K}_3] - U \end{pmatrix} \quad (1)$$

where $(\vec{K}_1, \vec{K}_2, \vec{K}_3) = (k_\theta, 0, -k_\theta)\hat{y}$, with $k_\theta = \frac{8\pi}{3a_0} \sin(\theta/2)$ and $a_0 = 0.246\text{ nm}$, and $\vec{\sigma}_\theta = e^{-i\theta\sigma_z}(\sigma_x, \sigma_y)$ are Pauli matrices. The interlayer tunneling terms are

$$T(\vec{r}) = \begin{pmatrix} w_{AA}U_0(\vec{r}) & w_{AB}U_{-1}(\vec{r}) \\ w_{AB}U_1(\vec{r}) & w_{AA}\kappa U_0(\vec{r}) \end{pmatrix} \quad (2)$$

with $U_l(\vec{r}) = e^{i\vec{q}_0 \cdot \vec{r}} \sum_{n=0}^2 e^{\frac{2\pi i n}{3} l n} e^{-i\vec{q}_n \cdot \vec{r}}$, $q_{n,x} + iq_{n,y} = -ik_\theta e^{\frac{2\pi i}{3} n}$. The h-HTG and \bar{h} -HTG regions are modeled by choosing the displacements $\vec{d}_t - \vec{d}_b = \pm\vec{\delta}$ respectively, where $\vec{\delta} = \frac{1}{3}(\vec{a}_2 - \vec{a}_1)$, and $a_{1,2} = a_0(\pm\frac{\sqrt{3}}{2}, \frac{1}{2})$ are the atomic lattice vectors. The layer potential U models the effect of the displacement field, up to electrostatic corrections. We use parameters $v_0 = 8.8 \times 10^5 \text{ m/s}$, $w_{AB} = 110 \text{ meV}$, and $w_{AA} = 75 \text{ meV}$, and typically neglect the Pauli matrix rotation $\sigma_\theta \rightarrow \sigma$.

I. Microscopic parameters and valence band Van Hove singularity

We use the shape of the VHS on the hole doping side to estimate the value of the effective velocity ratio v_0/w_{AB} . Since the hole side ($n < 0$) does not show strong interaction effects in experiment, we can approximately treat the valence bands as non-interacting but with a renormalized velocity \tilde{v}_0 . The shape of the observed VHS can then be used to constrain the value of the \tilde{v}_0/w_{AB} .

Extended Data Fig. 9(left) shows the non-interacting density of states (DOS) calculated for the continuum model Eq. H as a function of filling factors $-4 < \nu < 0$ and U , for two choices of velocity: a “bare” velocity $v_0 = 0.88 \times 10^6 \text{ m/s}$ and a “renormalized” velocity $\tilde{v}_0 = 1.05 \times 10^6 \text{ m/s}$. The DOS shows multiple peaks corresponding to VHS arising from various Lifshitz transitions in the Fermi surface. To compare with Fig. 2b of the main text, we identify the changing sign of the Hall density with the VHS at which extended orbits exist in the Fermi surface [54]. Extended Data Fig. 9(right) shows the Fermi surfaces of the valence band as a function of filling factor at $U = 0$ and $U = 25 \text{ meV}$, which allow for the identification of the VHS with extended orbits, indicated by stars and the dashed lines in Extended Data Fig. 9(left).

The observed VHS for hole doping in Fig. 2b, which appears at $\nu \approx -0.8$ for $U = 0$, and moves to higher hole doping $\nu < -0.8$ in a displacement field, is therefore in better agreement with the theoretical model using an effective renormalized velocity \tilde{v}_0 .

J. Hartree-Fock calculations at $\nu = 7/2, 2/3$

In this section, we perform self-consistent Hartree-Fock calculations in moiré-periodic h-HTG at non-integer fillings $\nu = 7/2, 2/3$, the same fillings where correlated features were observed in Fig. 3. To the non-interacting Hamiltonian in Section H, we apply layer potentials $U, 0, -U$ on the three layers to mimic the effect of an external displacement field. Owing to the large energy gap to the remote bands, we project our calculations into the two central bands per flavour (spin and valley). We add dual-gate screened density-density interactions $V(q) = \frac{e^2}{2\epsilon_0\epsilon_r q} \tanh q d_{sc}$, where the gate screening length is $d_{sc} = 25 \text{ nm}$, and the effect of the hBN dielectric and remote bands is phenomenologically captured with the relative permittivity $\epsilon_r = 8$. The interaction term is normal-ordered with respect to the average density of the central bands at charge neutrality. To allow for gapped states at non-integer fillings within mean-field theory, we allow translation symmetry-breaking (TSB) by enlarging the unit cell. We allow breaking of all flavor and discrete rotational symmetries. Further details of the Hartree-Fock procedure are provided in Ref. [33].

At $\nu = 7/2$ (Extended Data Fig. 10a-f), we additionally let the system break translation symmetry by doubling the unit cell length along both moiré axes (quadrupling the area of the unit cell). We find that the lowest energy solution is a gapped state with TSB, as shown by the negative value of ΔE , which is defined as the Hartree-Fock energy per moiré unit cell, measured relative to the best translation-symmetric solution. Its density matrix is consistent with fully filling all bands, except a $|C| = 2$ band (corresponding to a B sublattice band in h-HTG) which

is half-filled and reconstructed by TSB and spatially-dependent spin rotations. While the charge density is moiré-periodic (Extended Data Fig. 10a), the quadrupling of the unit cell is revealed by the non-coplanar spin texture (Extended Data Fig. 10b) which forms a tetrahedral antiferromagnet (AFM), similar to that theoretically proposed in twisted monolayer-bilayer graphene (TMBG) and twisted double bilayer graphene (TDBG) in Ref. [55]. If we restrict the calculation to maintain spin-collinearity, we find two other spin-polarized solutions that realize a C_{3z} -symmetric CDW and a stripe CDW respectively (Extended Data Fig. 10c-d). The stripe CDW is reminiscent to that proposed in Ref. [10] to explain transport experiments in TMBG. All three solutions are $|C| = 1$ states that preserve valley $U(1)_V$ symmetry, and closely resemble the candidate ‘strong-coupling’ TSB orders expected from half-filling an ideal $|C| = 2$ band [47, 55]. The close energetic competition between the different orders (Extended Data Fig. 10e) points towards the ideality of the topological bands in h-HTG. $|\Delta E|$ decreases monotonically as a function of U , suggesting that the TSB state is weakened in a displacement field, though the U -dependence of the charge gap is less consistent (Extended Data Fig. 10f). While the TSB solutions remain energetically favoured for the large range of interlayer potentials studied, we caution that Hartree-Fock tends to overestimate gaps and symmetry-breaking, such that beyond mean-field theory, the threshold value of U where the system recovers symmetry is expected to be reduced.

In Extended Data Fig. 10g-h, we show analogous results for $\nu = 2/3$, where we allow translation symmetry-breaking to enlarge the unit cell threefold along both moiré axes. We again find the presence of gapped TSB solutions, though the gap size and TSB energy gain $|\Delta E|$ are smaller and non-monotonic in U . Interestingly, we find a window of non-zero interlayer potentials, slightly above/at the theoretical topological transition for $\nu = 1$ [33], where $|\Delta E|$ is locally maximal and the HF gap remains large. This suggests the possibility of a correlated state that only emerges at a nonzero displacement field. However, the presence of several closely-competing states, multiple partially filled flavors, and sensitive dependence on system parameters prevent an unambiguous interpretation of the Hartree-Fock results. We leave a more detailed theoretical investigation of the correlated physics at $\nu = 2/3$ to future work.

K. Magnetization reversal

In this section, we show using a theoretical model that the orbital magnetization of h-HTG switches sign as the density is tuned across the correlated insulating gap at $\nu = 3$. This explains the density-induced magnetization switching observed in Fig. 4, similar to the Chern mosaic in hBN-aligned MATBG [34].

In Extended Data Fig. 11(left), we show the self-consistent Hartree-Fock band structure at $\nu = 3$. The self-consistent calculation is performed including the remote bands. The single-particle bands are shown in the dashed lines. We observe that each of the filled bands is (quite rigidly) shifted, with the filled bands being shifted down by $\Delta_- \approx 20$ meV, and the unfilled band being shifted up by $\Delta_+ \approx 30$ meV, while the remote bands remain mostly unchanged [33]. In this case, the unfilled band is the (valley,spin,Chern-sublattice)=(K' , \downarrow , A) band.

To demonstrate the switching of orbital magnetization, we consider a simplified model following the Hartree-Fock bands. We assume the remote bands are perfectly rigid, and model the interaction-induced band shifting by a term $\Delta_- P + \Delta_+(1 - P)$, where P is a (momentum-dependent) projector to the filled Chern-sublattice-basis bands in the flat band manifold, which rigidly shifts the filled bands by $\Delta_- = -20$ meV and unfilled bands by $\Delta_+ = 30$ meV. The orbital magnetization can then be computed as a function of the chemical potential μ (which can be arbitrary, but is only realistic if it also corresponds to the physical density $\nu = 3$), given by Ref. [35]

$$M_{\text{orb}} = -\frac{e}{\hbar} \sum_n \int \frac{d^2k}{4\pi^2} f(E_n(k) - \mu) \sum_{m \neq n} \text{Im} \frac{\langle n(k) | \partial_{k_x} H | m(k) \rangle \langle m(k) | \partial_{k_y} H | n(k) \rangle}{(E_n(k) - E_m(k))^2} \times [(E_n(k) - E_m(k)) + 2(\mu - E_n(k))] \quad (3)$$

where $|n(k)\rangle$ are the Bloch wavefunctions at k , n, m vary over all band indices (not just those in the flat band manifold), $E_n(k)$ is the energy of the n th band, and $f(x) = (1 + e^{\beta x})^{-1}$ is the Fermi function. Because P leaves the remote bands unchanged, the contribution to the magnetization from bands far from the Fermi energy vanishes. Equivalently, this can be written

$$M_{\text{orb}} = -\frac{e}{\hbar} \sum_n \int \frac{d^2k}{4\pi^2} f(E_n(k) - \mu) \sum_{m \neq n} \text{Im} (\partial_{k_x} n(k) | (E_n(k) - H) + 2(\mu - E_n(k)) | \partial_{k_y} n(k)) \quad (4)$$

Importantly, M_{orb} depends on μ even in the gap, due to contributions from the edge modes to the orbital magnetization. This allows M_{orb} to be discontinuous and flip sign when the density is tuned from just below to just above $\nu = 3$.

In Extended Data Fig. 11(right), we show the orbital magnetization as a function of the filling factor ν . We use a 60×60 discretization of the moiré Brillouin zone and $\beta^{-1} = 0.2$ meV. The orbital magnetization is discontinuous

and indeed switches sign from negative to positive at $\nu = 3$. In addition to the state studied here, there is also the time-reversed partner which has opposite M_{orb} . The energetic competition between these two states in an applied magnetic field can therefore be affected by tuning density to directly above/below the $\nu = 3$ gap.

L. Relaxation

To calculate the relaxation of the HTG system, we employ a continuum relaxation model in local configuration space [56]. Therefore, instead of formulating the problem in real space, we adopt configuration space, which describes the local environment of every position in layer L_ℓ and bypasses a periodic approximation [57]. Every position in real space \vec{r} in L_i can be uniquely parametrized by three shift vectors $\vec{b}^{i \rightarrow j}$ for $j = 1, 2, 3$ that describes the relative position between any point in real space \vec{r} with respect to all three layers. Note that $\vec{b}^{i \rightarrow j} = \vec{0}$ if $i = j$ since the separation between a position with itself is 0, which leads to a four-dimensional configuration space.

For a given real space position \vec{r} , the following linear transformation uniquely maps between the real space position, \vec{r} , and the local configuration space component in layer i with respect to layer j $\vec{b}^{i \rightarrow j}$:

$$\vec{b}^{i \rightarrow j}(\vec{r}) = (E_j^{-1} E_i - \mathbb{1}) \vec{r}, \quad (5)$$

where E_i and E_j are the unit cell vectors of layers i and j respectively, rotated by θ_{ij} . In the trilayer system, there is no simple linear transformation between real and configuration space. The relation between the displacement field defined in real space, $\vec{U}^{(i)}(\vec{r})$, and in configuration space, $\vec{u}^{(i)}(\vec{b})$, can be found by evaluating $\vec{u}^{(j)}(\vec{b})$ at the corresponding $\vec{b}^{i \rightarrow j}(\vec{r})$ and $\vec{b}^{i \rightarrow k}(\vec{r})$ with Eq. (5) to obtain

$$\vec{U}^{(i)}(\vec{r}) = \vec{u}^{(i)}(\vec{b}^{i \rightarrow j}(\vec{r}), \vec{b}^{i \rightarrow k}(\vec{r})), \quad (6)$$

where $j, k \neq i$ and $j < k$.

The relaxed energy has two contributions, intralayer and interlayer energies:

$$E^{\text{tot}}(\vec{u}^{(1)}, \vec{u}^{(2)}, \vec{u}^{(3)}) = E^{\text{intra}}(\vec{u}^{(1)}, \vec{u}^{(2)}, \vec{u}^{(3)}) + E^{\text{inter}}(\vec{u}^{(1)}, \vec{u}^{(2)}, \vec{u}^{(3)}), \quad (7)$$

where $\vec{u}^{(\ell)}$ is the relaxation displacement vector in layer ℓ . To obtain the relaxation pattern, we minimize the total energy with respect to the relaxation displacement vector.

We model the intralayer coupling based on linear elasticity theory:

$$\begin{aligned} E^{\text{intra}}(\vec{u}^{(1)}, \vec{u}^{(2)}, \vec{u}^{(3)}) = & \sum_{\ell=1}^3 \int \frac{1}{2} \left[G(\partial_x u_x^{(\ell)} + \partial_y u_y^{(\ell)})^2 \right. \\ & \left. + K((\partial_x u_x^{(\ell)} - \partial_y u_y^{(\ell)})^2 + (\partial_x u_y^{(\ell)} + \partial_y u_x^{(\ell)})^2) \right] d\vec{b}, \end{aligned} \quad (8)$$

where G and K are shear and bulk moduli of monolayer graphene, which we take to be $G = 47352 \text{ meV}/\text{unit cell}$, $K = 69518 \text{ meV}/\text{unit cell}$ [56, 58].

The interlayer energy accounts for the energy cost of the layer misfit, which is described by the generalized stacking fault energy (GSFE) [59, 60], obtained using first principles Density Functional Theory (DFT) with the Vienna Ab initio Simulation Package (VASP) [61–63]. GSFE is the ground state energy as a function of the local stacking with respect to the lowest energy stacking between a bilayer. For bilayer graphene, GSFE is maximized at the AA stacking and minimized at the AB stacking. Letting $\vec{b} = (b_x, b_y)$ be the relative stacking between two layers, we define the following vector $\vec{v} = (v, w) \in [0, 2\pi]^2$:

$$\begin{pmatrix} v \\ w \end{pmatrix} = \frac{2\pi}{a_0} \begin{bmatrix} \sqrt{3}/2 & -1/2 \\ \sqrt{3}/2 & 1/2 \end{bmatrix} \begin{pmatrix} b_x \\ b_y \end{pmatrix}, \quad (9)$$

where $a_0 = 2.4595 \text{ \AA}$ is the graphene lattice constant. We parameterize the GSFE as follows,

$$\begin{aligned} V_{j\pm}^{\text{GSFE}} = & c_0 + c_1(\cos v + \cos w + \cos(v + w)) \\ & + c_2(\cos(v + 2w) + \cos(v - w) + \cos(2v + w)) \\ & + c_3(\cos(2v) + \cos(2w) + \cos(2v + 2w)), \end{aligned} \quad (10)$$

where we take $c_0 = 6.832 \text{ meV}/\text{cell}$, $c_1 = 4.064 \text{ meV}/\text{cell}$, $c_2 = -0.374 \text{ meV}/\text{cell}$, $c_3 = -0.0095 \text{ meV}/\text{cell}$ [56, 58]. The van der Waals force is implemented through the vdW-DFT method using the SCAN+rVV10 functional [64]. In terms of

$V_{\ell\pm}^{\text{GSFE}}$, the total interlayer energy can be expressed as follows:

$$E^{\text{inter}} = \frac{1}{2} \int V_{1+}^{\text{GSFE}}(\vec{B}^{1\rightarrow 2}) d\vec{b} + \frac{1}{2} \int [V_{2-}^{\text{GSFE}}(\vec{B}^{2\rightarrow 1}) + V_{2+}^{\text{GSFE}}(\vec{B}^{2\rightarrow 3})] d\vec{b} \\ + \frac{1}{2} \int V_{3-}^{\text{GSFE}}(\vec{B}^{3\rightarrow 2}) d\vec{b},$$

where $\vec{B}^{i\rightarrow j} = \vec{b}^{i\rightarrow j} + \vec{u}^{(j)} - \vec{u}^{(i)}$ is the relaxation modified local shift vector. Note that we neglect the interlayer coupling between layers 1 and 3. The total energy is obtained by summing over uniformly sampled configuration space. In this work, we discretize the four-dimensional configuration space by $54 \times 54 \times 54 \times 54$.

M. Unequal twist angles

We show the relaxed supermoiré structure calculated for unequal twist angles $(\theta, 0, -\theta')$. Extended Data Fig. 12 shows the local misfit energy for $\theta = 1.8^\circ$ with varying $\theta' = 1.8^\circ, 1.75^\circ, 1.7^\circ$. The h-HTG and \bar{h} -HTG domains can be identified by the honeycomb pattern in the misfit energy. It can be seen that the local physics within the h-HTG and \bar{h} -HTG domains remain relatively unchanged, meaning that the structure locally relaxes into the equal-angle commensurate configuration. Thus, the main effect of the angle difference is the reduction of the domain size (which is determined by the supermoiré period of the unrelaxed structure).

ACKNOWLEDGMENTS

We thank M. Kastner and P. Ledwith for helpful discussions, A. Bangura, G. Jones, R. Nowell, A. Woods, and S. Hannahs for technical support, and X. Wang for assistance with device fabrication. This work was partially supported by the Army Research Office MURI W911NF2120147, the 2DMAGIC MURI FA9550-19-1-0390, the National Science Foundation (DMR-1809802), the STC Center for Integrated Quantum Materials (NSF grant no. DMR-1231319), and the Gordon and Betty Moore Foundation's EPiQS Initiative through grant GBMF9463 to PJH. This work was supported by the Air Force Office of Scientific Research (AFOSR) under award FA9550-22-1-0432. Measurement infrastructure was funded in part by the Gordon and Betty Moore Foundation's EPiQS initiative through grant GBMF3429 and grant GBMF9460. D.G.-G. gratefully acknowledges support from the Ross M. Brown Family Foundation. K.W. and T.T. acknowledge support from the JSPS KAKENHI (Grant Numbers 21H05233 and 23H02052) and World Premier International Research Center Initiative (WPI), MEXT, Japan. A portion of this work was performed at the National High Magnetic Field Laboratory, which is supported by National Science Foundation Cooperative Agreement No. DMR-2128556 and the State of Florida. This work was performed in part at the Harvard University Center for Nanoscale Systems (CNS); a member of the National Nanotechnology Coordinated Infrastructure Network (NNCI), which is supported by the National Science Foundation under NSF award no. ECCS-2025158. This work was carried out in part through the use of MIT.nano's facilities. This work made use of the MRSEC Shared Experimental Facilities at MIT, supported by the National Science Foundation under award number DMR-1419807. AU acknowledges support from the MIT Pappalardo Fellowship and from the VATAT Outstanding Postdoctoral Fellowship in Quantum Science and Technology. ZZ is supported by a Stanford Science fellowship. Sandia National Laboratories is a multimission laboratory managed and operated by National Technology & Engineering Solutions of Sandia, LLC, a wholly owned subsidiary of Honeywell International Inc., for the U.S. Department of Energy's National Nuclear Security Administration under contract DE-NA000352.

AUTHOR CONTRIBUTIONS

S.C.d.l.B., and A.U. conceived the project. L.-Q.X. fabricated the devices with the help of A.U.. L.-Q.X., A.U. and S.C.d.l.B. carried out the helium-3 transport measurements. A.S. and L.-Q.X. carried out the dilution fridge transport measurements under the supervision of D.G.-G.. T.D. and Y.H.K. performed band structure, magnetization and Hartree-Fock calculations. T.D. and Z.Z performed lattice relaxation calculations. K.W. and T.T. supplied the boron nitride crystals. A.U., S.C.d.l.B., L.-Q.X., A.S., T.D., L.F., and P.J-H. analyzed the data and discussed the interpretation. A.U., S.C.d.l.B., and L.-Q.X. wrote the manuscript with input from all authors. P.J.-H. supervised the project.

COMPETING INTERESTS

The authors declare no competing interests.

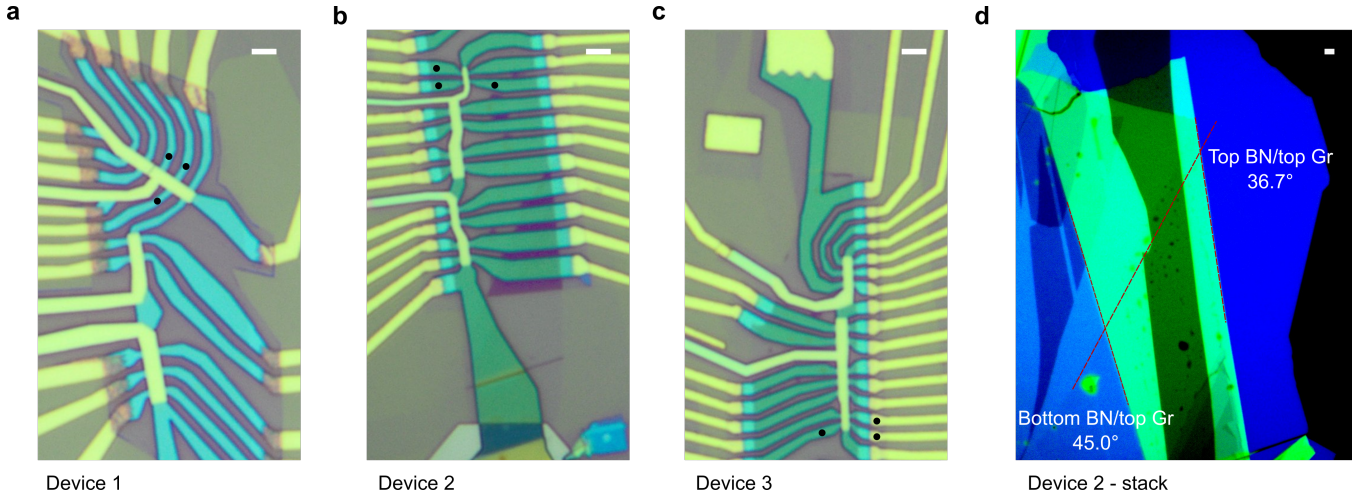
DATA AVAILABILITY

The data that support the findings of this study are available from the corresponding authors upon reasonable request.

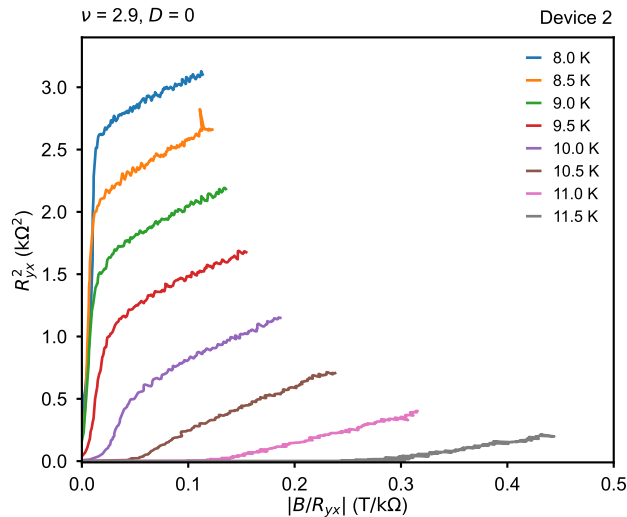
- [1] N. Nagaosa, J. Sinova, S. Onoda, A. H. MacDonald, and N. P. Ong, Anomalous Hall effect, *Rev. Mod. Phys.* **82**, 1539 (2010).
- [2] A. L. Sharpe, E. J. Fox, A. W. Barnard, J. Finney, K. Watanabe, T. Taniguchi, M. A. Kastner, and D. Goldhaber-Gordon, Emergent ferromagnetism near three-quarters filling in twisted bilayer graphene, *Science* **365**, 605 (2019).
- [3] M. Serlin, C. L. Tschirhart, H. Polshyn, Y. Zhang, J. Zhu, K. Watanabe, T. Taniguchi, L. Balents, and A. F. Young, Intrinsic quantized anomalous Hall effect in a moiré heterostructure, *Science* **367**, 900 (2020).
- [4] G. Chen, A. L. Sharpe, E. J. Fox, Y.-H. Zhang, S. Wang, L. Jiang, B. Lyu, H. Li, K. Watanabe, T. Taniguchi, Z. Shi, T. Senthil, D. Goldhaber-Gordon, Y. Zhang, and F. Wang, Tunable correlated Chern insulator and ferromagnetism in a moiré superlattice, *Nature* **579**, 56 (2020).
- [5] H. Polshyn, J. Zhu, M. A. Kumar, Y. Zhang, F. Yang, C. L. Tschirhart, M. Serlin, K. Watanabe, T. Taniguchi, A. H. MacDonald, and A. F. Young, Electrical switching of magnetic order in an orbital Chern insulator, *Nature* **588**, 66 (2020).
- [6] S. Chen, M. He, Y.-H. Zhang, V. Hsieh, Z. Fei, K. Watanabe, T. Taniguchi, D. H. Cobden, X. Xu, C. R. Dean, and M. Yankowitz, Electrically tunable correlated and topological states in twisted monolayer–bilayer graphene, *Nature Physics* **17**, 374 (2021).
- [7] C. L. Tschirhart, M. Serlin, H. Polshyn, A. Shragai, Z. Xia, J. Zhu, Y. Zhang, K. Watanabe, T. Taniguchi, M. E. Huber, and A. F. Young, Imaging orbital ferromagnetism in a moiré Chern insulator, *Science* **372**, 1323 (2021).
- [8] M. He, Y.-H. Zhang, Y. Li, Z. Fei, K. Watanabe, T. Taniguchi, X. Xu, and M. Yankowitz, Competing correlated states and abundant orbital magnetism in twisted monolayer–bilayer graphene, *Nature Communications* **12**, 4727 (2021).
- [9] P. Stepanov, M. Xie, T. Taniguchi, K. Watanabe, X. Lu, A. H. MacDonald, B. A. Bernevig, and D. K. Efetov, Competing zero-field Chern insulators in superconducting twisted bilayer graphene, *Phys. Rev. Lett.* **127**, 197701 (2021).
- [10] H. Polshyn, Y. Zhang, M. A. Kumar, T. Soejima, P. Ledwith, K. Watanabe, T. Taniguchi, A. Vishwanath, M. P. Zaletel, and A. F. Young, Topological charge density waves at half-integer filling of a moiré superlattice, *Nature Physics* **18**, 42 (2022).
- [11] C. Zhang, T. Zhu, T. Soejima, S. Kahn, K. Watanabe, T. Taniguchi, A. Zettl, F. Wang, M. P. Zaletel, and M. F. Crommie, Local spectroscopy of a gate-switchable moiré quantum anomalous Hall insulator, *Nature Communications* **14**, 3595 (2023).
- [12] C.-C. Tseng, X. Ma, Z. Liu, K. Watanabe, T. Taniguchi, J.-H. Chu, and M. Yankowitz, Anomalous Hall effect at half filling in twisted bilayer graphene, *Nature Physics* **18**, 1038 (2022).
- [13] M. Kuri, C. Coleman, Z. Gao, A. Vishnuradhan, K. Watanabe, T. Taniguchi, J. Zhu, A. H. MacDonald, and J. Folk, Spontaneous time-reversal symmetry breaking in twisted double bilayer graphene, *Nature Communications* **13**, 6468 (2022).
- [14] M. He, J. Cai, Y.-H. Zhang, Y. Liu, Y. Li, T. Taniguchi, K. Watanabe, D. H. Cobden, M. Yankowitz, and X. Xu, Chirality-dependent topological states in twisted double bilayer graphene (2021), [arXiv:2109.08255 \[cond-mat.mes-hall\]](https://arxiv.org/abs/2109.08255).
- [15] N. J. Zhang, J.-X. Lin, Y. Wang, K. Watanabe, T. Taniguchi, L. Fu, and J. I. A. Li, Valley ferromagnetism and superconductivity in magic-angle trilayer graphene (2023), [arXiv:2209.12964 \[cond-mat.mes-hall\]](https://arxiv.org/abs/2209.12964).
- [16] T. Li, S. Jiang, B. Shen, Y. Zhang, L. Li, Z. Tao, T. Devakul, K. Watanabe, T. Taniguchi, L. Fu, J. Shan, and K. F. Mak, Quantum anomalous Hall effect from intertwined moiré bands, *Nature* **600**, 641 (2021).
- [17] J.-X. Lin, Y.-H. Zhang, E. Morissette, Z. Wang, S. Liu, D. Rhodes, K. Watanabe, T. Taniguchi, J. Hone, and J. I. A. Li, Spin-orbit-driven ferromagnetism at half moiré filling in magic-angle twisted bilayer graphene, *Science* **375**, 437 (2022).
- [18] R. Polski, Y. Zhang, Y. Peng, H. S. Arora, Y. Choi, H. Kim, K. Watanabe, T. Taniguchi, G. Refael, F. von Oppen, and S. Nadj-Perge, Hierarchy of symmetry breaking correlated phases in twisted bilayer graphene (2022), [arXiv:2205.05225 \[cond-mat.str-el\]](https://arxiv.org/abs/2205.05225).
- [19] G. Chen, A. L. Sharpe, E. J. Fox, S. Wang, B. Lyu, L. Jiang, H. Li, K. Watanabe, T. Taniguchi, M. F. Crommie, M. A. Kastner, Z. Shi, D. Goldhaber-Gordon, Y. Zhang, and F. Wang, Tunable orbital ferromagnetism at noninteger filling of a moiré superlattice, *Nano Letters* **22**, 238 (2022).
- [20] E. Anderson, F.-R. Fan, J. Cai, W. Holtzmann, T. Taniguchi, K. Watanabe, D. Xiao, W. Yao, and X. Xu, Programming correlated magnetic states with gate-controlled moiré geometry, *Science* **381**, 325 (2023).
- [21] J. Cai, E. Anderson, C. Wang, X. Zhang, X. Liu, W. Holtzmann, Y. Zhang, F. Fan, T. Taniguchi, K. Watanabe, Y. Ran, T. Cao, L. Fu, D. Xiao, W. Yao, and X. Xu, Signatures of fractional quantum anomalous Hall states in twisted MoTe₂, *Nature* [10.1038/s41586-023-06289-w](https://doi.org/10.1038/s41586-023-06289-w) (2023).

- [22] Y. Zeng, Z. Xia, K. Kang, J. Zhu, P. Knüppel, C. Vaswani, K. Watanabe, T. Taniguchi, K. F. Mak, and J. Shan, Thermodynamic evidence of fractional Chern insulator in moiré MoTe₂, *Nature* **10.1038/s41586-023-06452-3** (2023).
- [23] B. A. Foutty, C. R. Kometter, T. Devakul, A. P. Reddy, K. Watanabe, T. Taniguchi, L. Fu, and B. E. Feldman, Mapping twist-tuned multi-band topology in bilayer wse₂ (2023), [arXiv:2304.09808 \[cond-mat.mes-hall\]](#).
- [24] H. Park, J. Cai, E. Anderson, Y. Zhang, J. Zhu, X. Liu, C. Wang, W. Holtzmann, C. Hu, Z. Liu, T. Taniguchi, K. Watanabe, J.-h. Chu, T. Cao, L. Fu, W. Yao, C.-Z. Chang, D. Cobden, D. Xiao, and X. Xu, Observation of fractionally quantized anomalous Hall effect, *Nature* **10.1038/s41586-023-06536-0** (2023).
- [25] F. Xu, Z. Sun, T. Jia, C. Liu, C. Xu, C. Li, Y. Gu, K. Watanabe, T. Taniguchi, B. Tong, J. Jia, Z. Shi, S. Jiang, Y. Zhang, X. Liu, and T. Li, Observation of integer and fractional quantum anomalous Hall states in twisted bilayer MoTe₂ (2023), [arXiv:2308.06177 \[cond-mat.mes-hall\]](#).
- [26] C. Mora, N. Regnault, and B. A. Bernevig, Flatbands and perfect metal in trilayer moiré graphene, *Phys. Rev. Lett.* **123**, 026402 (2019).
- [27] Y. Mao, D. Guerci, and C. Mora, Supermoiré low-energy effective theory of twisted trilayer graphene, *Phys. Rev. B* **107**, 125423 (2023).
- [28] F. K. Popov and G. Tarnopolsky, Magic angles in equal-twist trilayer graphene (2023), [arXiv:2303.15505 \[cond-mat.str-el\]](#).
- [29] T. Devakul, P. J. Ledwith, L.-Q. Xia, A. Uri, S. C. de la Barrera, P. Jarillo-Herrero, and L. Fu, Magic-angle helical trilayer graphene, *Science Advances* **9**, eadi6063 (2023).
- [30] D. Guerci, Y. Mao, and C. Mora, Chern mosaic and ideal flat bands in equal-twist trilayer graphene (2023), [arXiv:2305.03702 \[cond-mat.mes-hall\]](#).
- [31] N. Nakatsuji, T. Kawakami, and M. Koshino, Multiscale lattice relaxation in general twisted trilayer graphenes, *Phys. Rev. X* **13**, 041007 (2023).
- [32] D. Guerci, Y. Mao, and C. Mora, Nature of even and odd magic angles in helical twisted trilayer graphene (2023), [arXiv:2308.02638 \[cond-mat.mes-hall\]](#).
- [33] Y. H. Kwan, P. J. Ledwith, C. F. B. Lo, and T. Devakul, Strong-coupling topological states and phase transitions in helical trilayer graphene (2023), [arXiv:2308.09706 \[cond-mat.str-el\]](#).
- [34] S. Grover, M. Bocarsly, A. Uri, P. Stepanov, G. Di Battista, I. Roy, J. Xiao, A. Y. Meltzer, Y. Myasoedov, K. Pareek, K. Watanabe, T. Taniguchi, B. Yan, A. Stern, E. Berg, D. K. Efetov, and E. Zeldov, Chern mosaic and berry-curvature magnetism in magic-angle graphene, *Nature Physics* **18**, 885 (2022).
- [35] D. Xiao, M.-C. Chang, and Q. Niu, Berry phase effects on electronic properties, *Rev. Mod. Phys.* **82**, 1959 (2010).
- [36] A. Uri, S. C. de la Barrera, M. T. Randeria, D. Rodan-Legrain, T. Devakul, P. J. D. Crowley, N. Paul, K. Watanabe, T. Taniguchi, R. Lifshitz, L. Fu, R. C. Ashoori, and P. Jarillo-Herrero, Superconductivity and strong interactions in a tunable moiré quasicrystal, *Nature* **10.1038/s41586-023-06294-z** (2023).
- [37] D. C. W. Foo, Z. Zhan, M. M. A. Ezzi, L. Peng, S. Adam, and F. Guinea, Extended magic phase in twisted graphene multilayers (2023), [arXiv:2305.18080 \[cond-mat.str-el\]](#).
- [38] F. K. Popov and G. Tarnopolsky, Magic angle butterfly in twisted trilayer graphene (2023), [arXiv:2305.16385 \[cond-mat.str-el\]](#).
- [39] H. Yoo, R. Engelke, S. Carr, S. Fang, K. Zhang, P. Cazeaux, S. H. Sung, R. Hovden, A. W. Tsai, T. Taniguchi, K. Watanabe, G.-C. Yi, M. Kim, M. Luskin, E. B. Tadmor, E. Kaxiras, and P. Kim, Atomic and electronic reconstruction at the van der Waals interface in twisted bilayer graphene, *Nature Materials* **18**, 448 (2019).
- [40] Y. Cao, V. Fatemi, S. Fang, K. Watanabe, T. Taniguchi, E. Kaxiras, and P. Jarillo-Herrero, Unconventional superconductivity in magic-angle graphene superlattices, *Nature* **556**, 43 (2018).
- [41] U. Zondiner, A. Rozen, D. Rodan-Legrain, Y. Cao, R. Queiroz, T. Taniguchi, K. Watanabe, Y. Oreg, F. von Oppen, A. Stern, E. Berg, P. Jarillo-Herrero, and S. Ilani, Cascade of phase transitions and dirac revivals in magic-angle graphene, *Nature* **582**, 203 (2020).
- [42] D. Wong, K. P. Nuckolls, M. Oh, B. Lian, Y. Xie, S. Jeon, K. Watanabe, T. Taniguchi, B. A. Bernevig, and A. Yazdani, Cascade of electronic transitions in magic-angle twisted bilayer graphene, *Nature* **582**, 198 (2020).
- [43] J. M. Park, Y. Cao, K. Watanabe, T. Taniguchi, and P. Jarillo-Herrero, Tunable strongly coupled superconductivity in magic-angle twisted trilayer graphene, *Nature* **2021** 590:7845 **590**, 249 (2021).
- [44] C. Huang, N. Wei, and A. H. MacDonald, Current-driven magnetization reversal in orbital Chern insulators, *Phys. Rev. Lett.* **126**, 056801 (2021).
- [45] A. L. Sharpe, E. J. Fox, A. W. Barnard, J. Finney, K. Watanabe, T. Taniguchi, M. A. Kastner, and D. Goldhaber-Gordon, Evidence of orbital ferromagnetism in twisted bilayer graphene aligned to hexagonal boron nitride, *Nano Letters* **21**, 4299 (2021).
- [46] C. N. Lau, M. W. Bockrath, K. F. Mak, and F. Zhang, Reproducibility in the fabrication and physics of moiré materials, *Nature* **602**, 41 (2022).
- [47] J. Dong, P. J. Ledwith, E. Khalaf, J. Y. Lee, and A. Vishwanath, Many-body ground states from decomposition of ideal higher Chern bands: Applications to chirally twisted graphene multilayers, *Phys. Rev. Res.* **5**, 023166 (2023).
- [48] J. Zhu, J.-J. Su, and A. H. MacDonald, Voltage-controlled magnetic reversal in orbital Chern insulators, *Phys. Rev. Lett.* **125**, 227702 (2020).
- [49] R. Bistritzer and A. H. MacDonald, Moiré bands in twisted double-layer graphene, *Proceedings of the National Academy of Sciences* **108**, 12233 (2011).
- [50] L. Wang, I. Meric, P. Y. Huang, Q. Gao, Y. Gao, H. Tran, T. Taniguchi, K. Watanabe, L. M. Campos, D. A. Muller, J. Guo, P. Kim, J. Hone, K. L. Shepard, and C. R. Dean, One-dimensional electrical contact to a two-dimensional material, *Science* **342**, 614 (2013).
- [51] L. Spietz, J. Teufel, and R. J. Schoelkopf, A twisted pair cryogenic filter (2006), [arXiv:cond-mat/0601316 \[cond-mat.other\]](#).

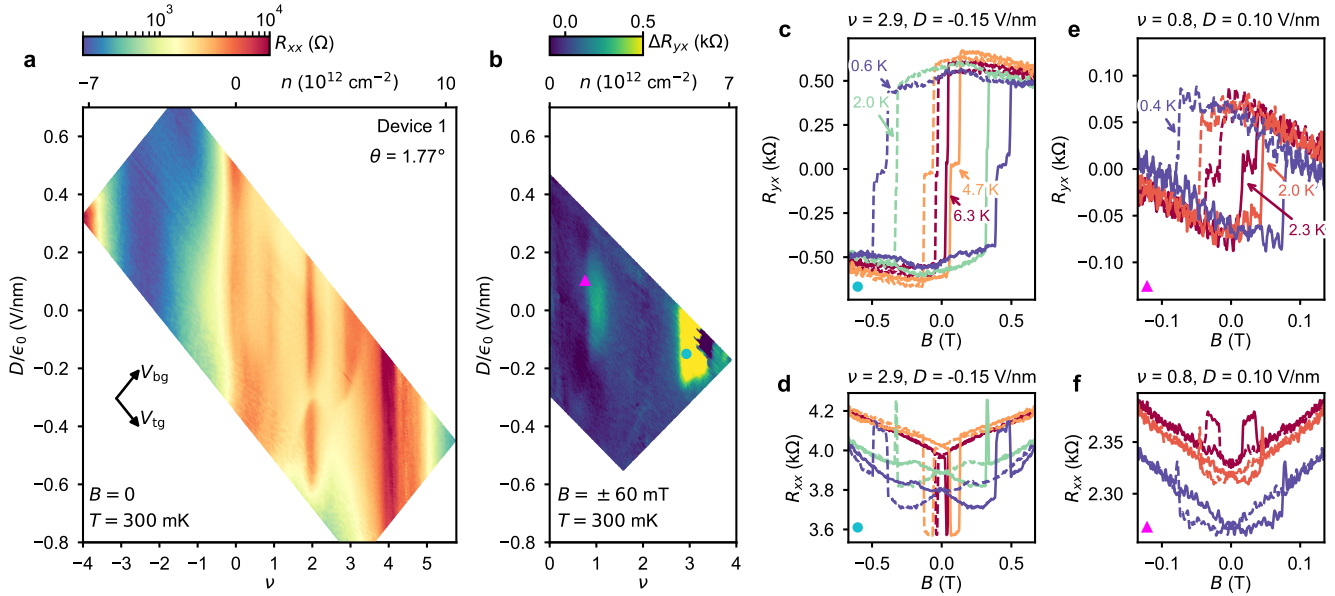
- [52] D. Chiba, S. Fukami, K. Shimamura, N. Ishiwata, K. Kobayashi, and T. Ono, Electrical control of the ferromagnetic phase transition in cobalt at room temperature, *Nature Materials* **2011** *10*:11 **10**, 853 (2011).
- [53] A. Arrott, Criterion for ferromagnetism from observations of magnetic isotherms, *Phys. Rev.* **108**, 1394 (1957).
- [54] N. W. Ashcroft and N. D. Mermin, *Solid state physics* (Cengage Learning, 2022).
- [55] P. H. Wilhelm, T. C. Lang, M. S. Scheurer, and A. M. Läuchli, Non-coplanar magnetism, topological density wave order and emergent symmetry at half-integer filling of moiré Chern bands, *SciPost Phys.* **14**, 040 (2023).
- [56] Z. Zhu, P. Cazeaux, M. Luskin, and E. Kaxiras, Modeling mechanical relaxation in incommensurate trilayer van der waals heterostructures, *Phys. Rev. B* **101**, 224107 (2020).
- [57] P. Cazeaux, M. Luskin, and D. Massatt, Energy minimization of two dimensional incommensurate heterostructures, *Archive for Rational Mechanics and Analysis* **235**, 1289 (2019), arXiv:1806.10395 [physics.comp-ph].
- [58] S. Carr, D. Massatt, S. B. Torrisi, P. Cazeaux, M. Luskin, and E. Kaxiras, Relaxation and domain formation in incommensurate two-dimensional heterostructures, *Phys. Rev. B* **98**, 224102 (2018).
- [59] E. Kaxiras and M. S. Duesbery, Free energies of generalized stacking faults in si and implications for the brittle-ductile transition, *Phys. Rev. Lett.* **70**, 3752 (1993).
- [60] S. Zhou, J. Han, S. Dai, J. Sun, and D. J. Srolovitz, Van der Waals bilayer energetics: Generalized stacking-fault energy of graphene, boron nitride, and graphene/boron nitride bilayers, *Phys. Rev. B* **92**, 155438 (2015).
- [61] G. Kresse and J. Hafner, Ab initio molecular dynamics for liquid metals, *Phys. Rev. B* **47**, 558 (1993).
- [62] G. Kresse and J. Furthmüller, Efficiency of ab initio total energy calculations for metals and semiconductors using a plane-wave basis set, *Computational Materials Science* **6**, 15 (1996).
- [63] G. Kresse and J. Furthmüller, Efficient iterative schemes for ab initio total-energy calculations using a plane-wave basis set, *Phys. Rev. B* **54**, 11169 (1996).
- [64] H. Peng, Z.-H. Yang, J. P. Perdew, and J. Sun, Versatile van der Waals density functional based on a meta-generalized gradient approximation, *Phys. Rev. X* **6**, 041005 (2016).



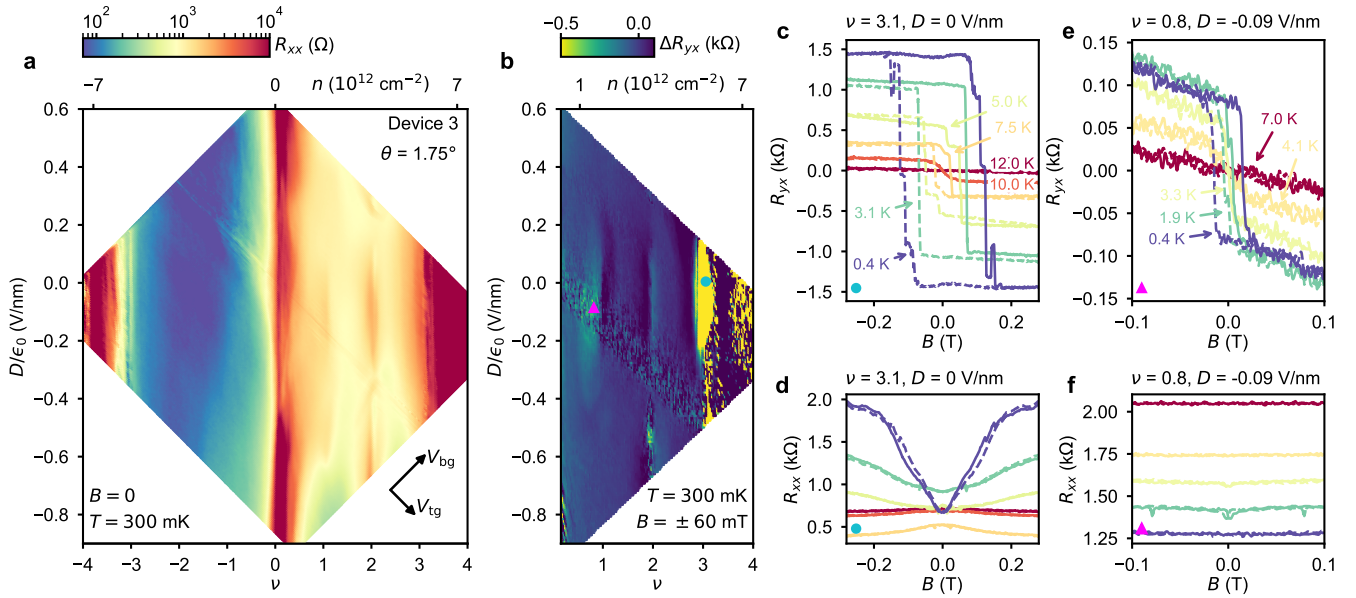
Extended Data Fig. 1. Optical micrographs of HTG devices. **a**, Device 1 – a secondary device with $\theta = 1.77^\circ$. **b**, Device 2 – our main device with $\theta = 1.79^\circ$. **c**, Device 3. This device shares the van der Waals heterostructure with Device 2. R_{xx} and R_{yx} contacts are indicated by black dots for all devices. **d**, Contrast-enhanced optical micrograph of Device 2 after stacking. The crystallographic edges of the top hBN, bottom hBN, and top monolayer graphene are highlighted, showing no accidental alignment between hBN and HTG. All scale bars are $2\ \mu\text{m}$.



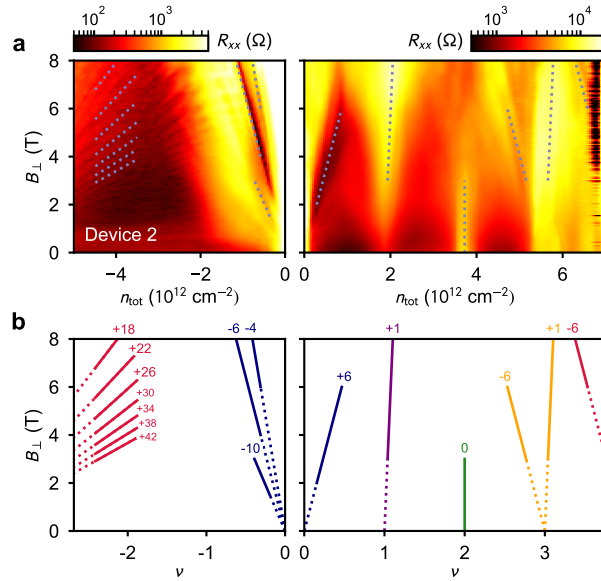
Extended Data Fig. 2. Extraction of the Curie temperature using an Arrott plot. R_{yx}^2 versus $|B/R_{yx}|$. positive (negative) extrapolated intercept of the linear part at high B indicates a ferromagnetic (paramagnetic) state. The curve taken at $T = 10.5\ \text{K}$ has approximately zero intercept, indicating a Curie temperature $T_C \approx 10.5\ \text{K}$



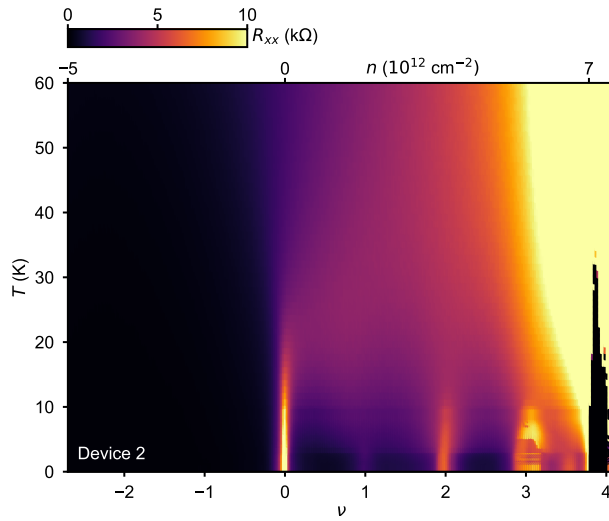
Extended Data Fig. 3. Device 1 characterization. **a**, R_{xx} versus n and D , showing resistance peaks at charge neutrality ($\nu = 0$), at the moiré band gaps ($\nu = \pm 4$), and at the correlated states at $\nu = 1, 2, 3$. **b**, Field-trained ΔR_{yx} measured at $T = 300$ mK and $B = \pm 60$ mT versus ν and D . Hot spots near $\nu = 1, 3$ indicate AHE. **c,d**, Field-antisymmetrized R_{yx} and field-symmetrized R_{xx} taken at $\nu = 2.9$ (cyan circle in **b**) and $D/\epsilon_0 = -0.15$ V/nm while sweeping B up (solid) and down (dashed) at different temperatures as indicated. Temperature colorcode in **d** is identical to **c**. **e,f**, Same as **c,d**, taken at $\nu = 0.8$ and $D/\epsilon_0 = 0.1$ V/nm (pink triangle in **b**).



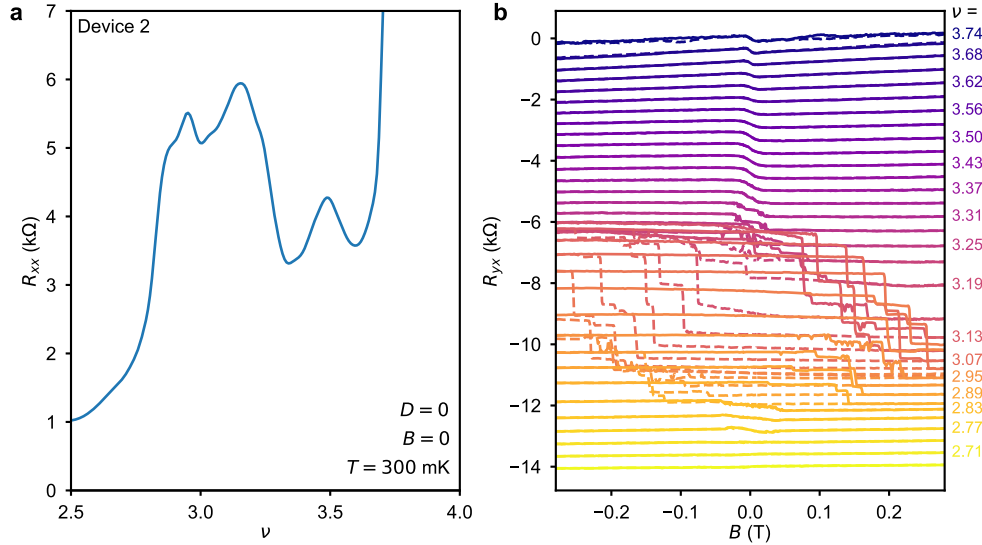
Extended Data Fig. 4. Device 3 characterization. **a**, R_{xx} versus n and D , showing resistance peaks at charge neutrality ($\nu = 0$), at the moiré band gaps ($\nu = \pm 4$), and at the correlated states at $\nu = 1, 2, 3$. The contact resistance becomes very large when $\nu \gtrsim 3.2$, leading to artifacts in the data. **b**, Field-trained ΔR_{yx} measured at $T = 300$ mK and $B = \pm 60$ mT versus ν and D . Hot spots near $\nu = 1, 3$ indicate AHE. **c,d**, Field-antisymmetrized R_{yx} and field-symmetrized R_{xx} taken at $\nu = 3.1$ (cyan circle in **b**) and $D/\epsilon_0 = 0$ while sweeping B up (solid) and down (dashed) at different temperatures as indicated. The temperature color code in **d** is identical to **c**. **e,f**, Same as **c,d**, taken at $\nu = 0.8$ and $D/\epsilon_0 = -0.09$ V/nm (pink triangle in **b**).



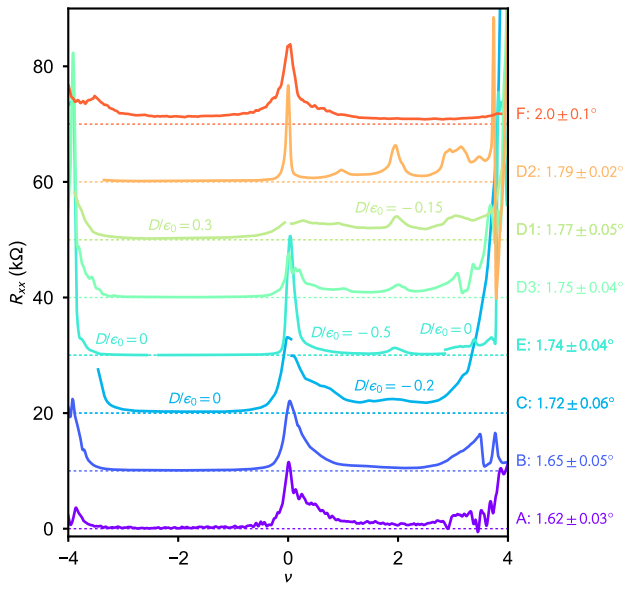
Extended Data Fig. 5. Twist angle determination. **a**, R_{xx} Landau fan from Device 2, measured at $D = 0$ and $T = 300$ mK. Electron-side (right) and hole-side (left) are plotted with different color scales to improve contrast. Dashed lines correspond to the best-fit series shown in **(b)**. **b**, Map of the best fit slopes from **(a)** emerging from a consistent set of integer fillings, ν . Red lines emerge from $n_{\nu=\pm 4}$ and $\nu = \pm 4$ (off-scale due to measurement limitations) in **(a)** and **(b)**, respectively.



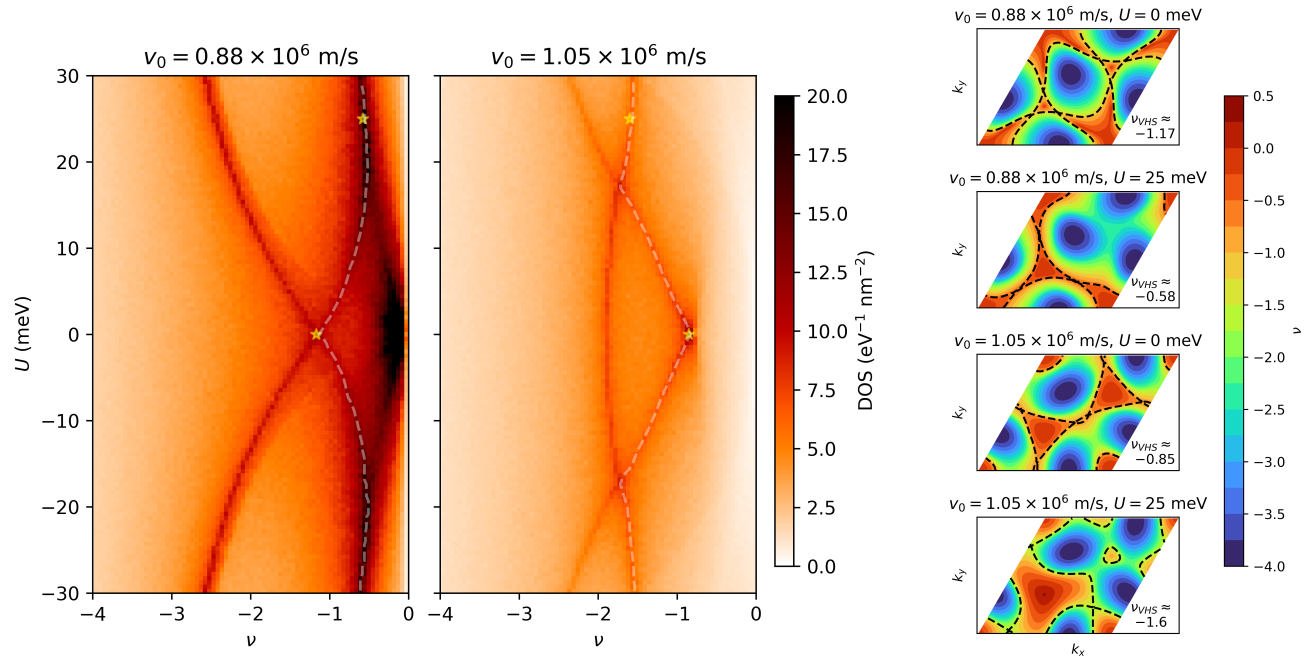
Extended Data Fig. 6. Temperature dependence. R_{xx} (raw data, not field-symmetrized) versus ν and T of Device 2 at $D = 0$ and $B = 0$. The jumps in resistance near $\nu = 3$ reflect the AHE of different magnetic states combined with R_{yx} mixing. A pronounced electron-hole asymmetry is demonstrated.



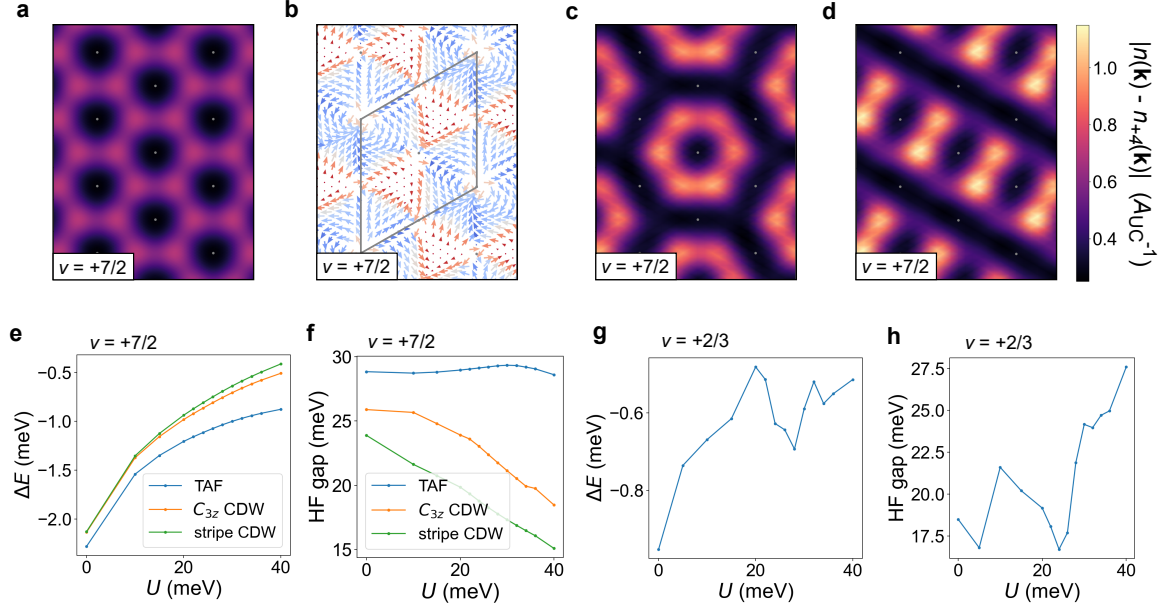
Extended Data Fig. 7. Correlated state at $\nu = 7/2$. **a**, R_{xx} versus ν , measured on Device 2 at $D = 0$, $B = 0$, and $T = 300 \text{ mK}$. At $\nu = 7/2$ we find a resistance peak distinct from the one at $\nu = 3$. **b**, Waterfall plot of antisymmetrized R_{yx} taken by sweeping B up (solid) and down (dashed) as the fast axis at $D = 0$ and different ν , as indicated on the right of every other curve. The AHE persists beyond $\nu = 7/2$.



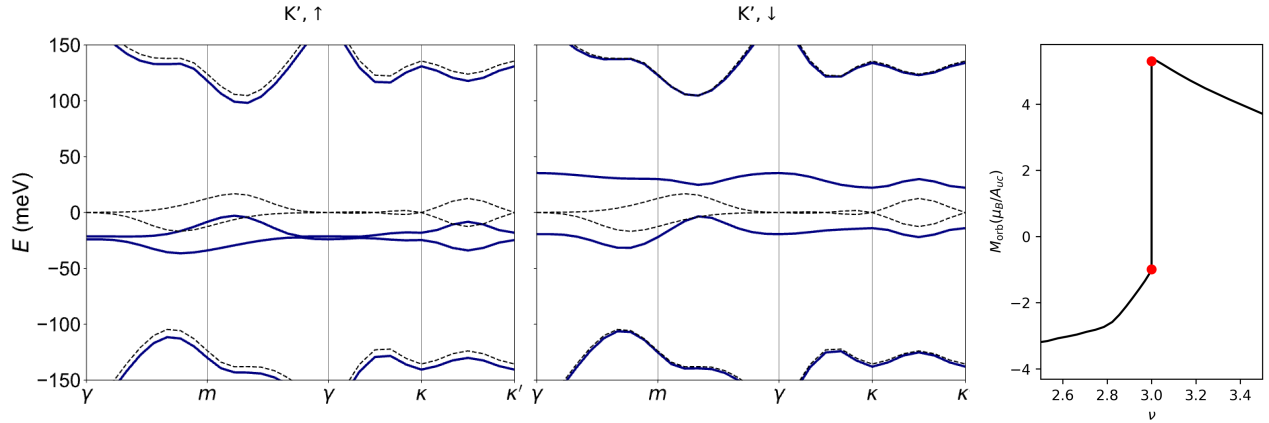
Extended Data Fig. 8. Twist angle dependence of R_{xx} features. Measured R_{xx} traces from devices with a range of twist angles, as summarized in Extended Data Table 2 (labels on the right correspond to entries in Extended Data Table 2). D1, D2, and D3 are equivalent to Devices 1, 2, and 3 shown in the paper, respectively. The traces were measured at a fixed D field, with $D = 0$ unless indicated otherwise (units are V/nm). The mean of the bounding estimates for the twist angle is used to label full filling, $|\nu| = 4$, for each curve.



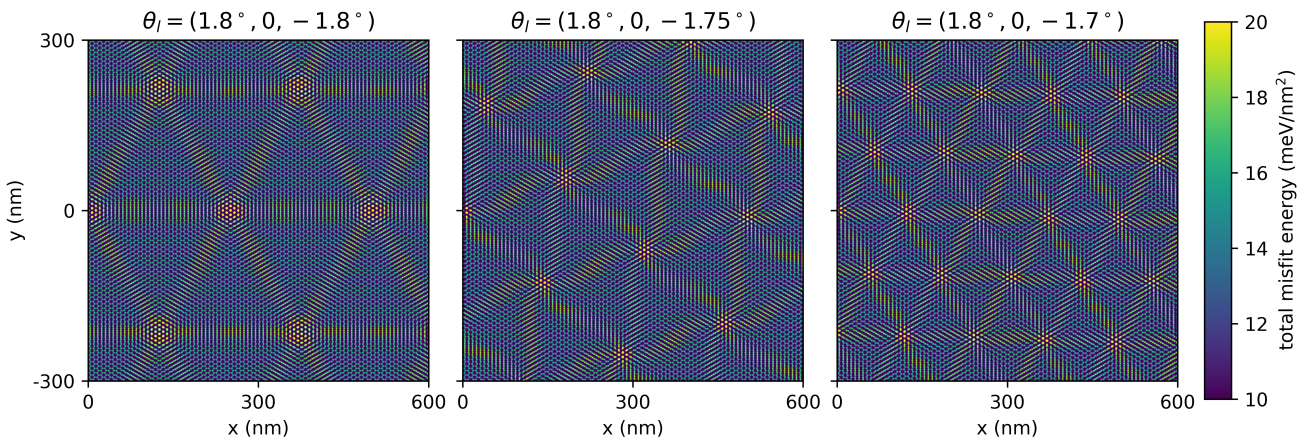
Extended Data Fig. 9. Single-particle density of states and Van Hove singularity. (left and center) The single particle DOS for hole doping as a function of filling factor and layer potential, for two velocity parameters v_0 . The VHS at which the Hall density switches sign is identified by the dashed lines. (right) Extended Fermi surfaces at the VHS are shown for the four points indicated by stars in the DOS plot.



Extended Data Fig. 10. Hartree-Fock calculations at $\nu = 7/2$ and $2/3$. **a**, Charge density $n(\mathbf{r})$ (measured relative to that at full flat band filling $n_{+4}(\mathbf{r})$) of the tetrahedral antiferromagnet (TAF) at $\nu = 7/2$. Grey dots indicate ABA-stacking regions. **b**, Local spin orientation in the TAF. Arrows denote spin direction in $s_x - s_y$ plane, while red (blue) coloring indicates out-of-plane polarization along $+\hat{s}_z$ ($-\hat{s}_z$). Grey parallelogram indicates the new quadrupoled moiré unit cell. **c,d** Same as **a** except for the \tilde{C}_{3z} CDW and stripe CDW respectively. **e**, ΔE of the different translation symmetry breaking solutions at $\nu = 7/2$ as a function of interlayer potential U . ΔE is measured relative to that of the best translation-symmetric solution. **f**, Charge gap of the translation symmetry breaking solutions at $\nu = 7/2$. **g,h**, Same as **e,f** except for the best translation symmetry breaking solution at $\nu = 2/3$. All calculations performed on a 18×18 system using $\theta = 1.80^\circ$, $w_{AA} = 75 \text{ meV}$.



Extended Data Fig. 11. Hartree-Fock bands and orbital magnetization at $\nu = 3$. (left and center) The HF quasiparticle bands at $\nu = 3$ are shown for the (K', \uparrow) (left) and (K', \downarrow) (center) sectors, with the non-interacting bands shown in dashed lines. The K valley bands are identical to the (K', \uparrow) , up to $k \rightarrow -k$. (right) The orbital magnetization, in units of Bohr magneton per moiré unit cell, calculated for the simplified model, showing a discontinuity and sign flip at $\nu = 3$ (red dots).



Extended Data Fig. 12. Relaxed structure for unequal twist angles. The interlayer misfit energy, summed over both layer pairs, is shown for HTG with angles $\theta_l = (\theta, 0, -\theta')$. The main effect of a small angle mismatch $\theta \neq \theta'$ is a reduction in the supermoiré domain size.

System	T_C (K)	Reference
Twisted bilayer MoTe ₂	14	[20, 21]
	13	[22]
	12	[24]
	10	[25]
HTG	10.5	This work
hBN-aligned MATBG	7.5	[3]
	5	[2]
tMBG	7	[5]
	2.5	[6]
WSe ₂ /MATBG	7	[17]
	5	[18]
AB-stacked MoTe ₂ /WSe ₂	5.5	[16]
Non-magic-angle twisted bilayer graphene	5.5	[12]
Near-commensurate hBN-MATBG superlattice	4.5	[9, 34]
hBN-aligned rhombohedral trilayer graphene	3.5	[4]
WSe ₂ /magic-angle twisted trilayer graphene	2.5	[15]
AB-AB stacked twisted double bilayer graphene	2.5	[13]
AB-BA stacked twisted double bilayer graphene	<2	[14]

Extended Data Table 1. Summary of AHE reported in moiré systems to date.

Label	Extracted angle	ν , correlated features	ν , AHE	e-h symmetry
A	$1.62 \pm 0.03^\circ$	-	-	Nearly symmetric
B	$1.65 \pm 0.05^\circ$	-	-	Nearly symmetric
C	$1.72 \pm 0.06^\circ$	2	-	Asymmetric
E	$1.74 \pm 0.04^\circ$	2,3	Unknown	Asymmetric
D3	$1.75 \pm 0.04^\circ$	1,2,3	1,3	Asymmetric
D1	$1.77 \pm 0.05^\circ$	1,2,3	1,3	Asymmetric
D2	$1.79 \pm 0.02^\circ$	1,2,3, $\frac{7}{2}$	$\frac{2}{3}, 1, 3$	Asymmetric
F	$2.0 \pm 0.1^\circ$	-	-	Nearly symmetric

Extended Data Table 2. Summary of twist angles with observed transport features.